Diagnostics and Testing of an Internal Osculating Waverider Inlet

Mark E. Noftz,* Andrew J. Shuck,† Joseph S. Jewell,‡ Jonathan Poggie,§
Purdue University, West Lafayette, IN, 47907, USA

Andrew N. Bustard,¶ Thomas J. Juliano‖
University of Notre Dame, Notre Dame, IN, 46556, USA

Nicholas J. Bisek**
Air Force Research Laboratory, Wright-Patterson AFB, OH, 45433, USA

The testing of an inward-turning, high-speed, 3D streamline traced inlet is presented from osculating axisymmetric theory. A new method of high-speed inlet design, labeled the Osculating Internal Waverider inlet with Parallel Streamlines (OIWPS), was used to design two inlet-isolator blockage models. These Indiana Inlet (INlet) models were tested in Purdue's Boeing-AFOSR Mach 6 Quiet Tunnel, where a Reynolds number sweep was conducted to investigate tunnel starting characteristics. Results informed the design of an appropriately-sized model for future experiments. Mean internal pressures are found to be considerably different between models, with the smaller version compressing the air much more effectively. Mass-injection back pressure studies were conducted to map the operational envelope of the inlet. Analyzed power spectra of Kulite sensors imply that cavity resonance is a prominent phenomena when the inlet sustains back pressurization. Finally, a methodology for a viscous correction is presented that will be included in future INlet models.

I. Nomenclature

AoA	=	Angle of Attack
$BAM6QT$	=	Boeing-AFOSR Mach 6 Quiet Tunnel
$BLVC$	=	Boundary Layer Viscous Correction
HF	=	Hot Film
$HIFiRE$	=	Hypersonic International Flight Research Experimentation Program
IML	=	Inner Mold Line
NWK	=	Nozzle Wall Kulite
PSD	=	Power Spectral Density
RMS	=	Root Mean Square
P_∞	=	Freestream Static Pressure
P_m	=	Mean Static Pressure
$R_\circ, h$	=	Isolator Height
Re_m	=	Freestream Unit Reynolds Number
β	=	Oblique Shock Angle
δ	=	Flow Deflection Angle
δ^*	=	Boundary Layer Displacement Thickness

*Graduate Student, School of Aeronautics and Astronautics, Student Member, AIAA, mnoftz@purdue.edu

†Graduate Student, School of Aeronautics and Astronautics, Student Member, AIAA

‡Assistant Professor, School of Aeronautics and Astronautics, Associate Fellow, AIAA

§Professor, School of Aeronautics and Astronautics, Associate Fellow, AIAA

¶Graduate Student, Department of Aerospace and Mechanical Engineering, Student Member, AIAA

‖Associate Professor, Department of Aerospace and Mechanical Engineering, Senior Member, AIAA

**Senior Research Aerospace Engineer, AFRL/RQHF, Associate Fellow, AIAA

II. Introduction

High speed inlets have a wide variety of applications within the fields of commercial travel and space access. The purpose of an inlet is to effectively capture and compress freestream air for efficient combustion. As freestream Mach number increases, mitigating stagnation pressure losses due to skin friction and shock waves become paramount design drivers. If a sufficiently large wetted area exists, then complex cooling requirements become necessary to handle the integrated heat loads. The inlet should also provide undisturbed, uniform flow entering the isolator for effective combustion. Most importantly, the inlet must avoid unstart, which is an aerodynamic phenomenon that drastically reduces mass capture and increases static pressure within the internal flowpath. During unstart, inlet capture characteristics are dependent on the internal flow within the duct [1]. The coupled nature of the problems make inlet design a challenging endeavor.

Simple two-dimensional ramp and axisymmetric inlets have been studied extensively in the open literature. Although they are easy to analyze, they lack compression efficiency and usually incorporate a high amount of on-design spillage [2]. Additionally, these inlets often feed directly into rectangular isolators, which are less structurally efficient and have higher drag and cooling requirements than round designs [3]. Therefore, for flight vehicles, it becomes desirable to create a three-dimensional inlet capable of creating a uniform flow into an elliptical or circular isolator. Over the last two decades, focus has shifted to these more advanced three-dimensional designs. Analysis tools and rapid prototyping have grown in functionality and precision, giving designers more freedom to create complex geometries. Inward-turning, streamline traced inlets are usually much shorter and lighter when compared against 2D geometries for equivalent flow compression ratios. Additionally, they are more easily integrated onto vehicles because of their tailored inlet shapes [4]. Other improved qualities include a decrease in overall drag, weaker cowl shocks that mitigate adverse shock-wave boundary layer interaction (SWBLI) effects, and smaller wetted areas that decrease heat loading. However, the improvements do come with some concerns. Since contraction ratios and mass capture efficiencies are higher, the starting characteristics of the inlet become problematic at off-design conditions [5]. Inward-turning designs often have to account for unfavorable starting scenarios by incorporating area relief, spill notches, and less aggressive internal contraction ratios.

The first step to designing an inlet is to select a compressive parent flowfield that will capture freestream air and compress it to the desired static pressure and Mach number. One such parent flowfield is the classic Busemann diffuser. Originally conceived of by Busemann and described by Mölder, this axisymmetric flowfield is capable of very efficient compression at supersonic Mach numbers [6]. A diagram of the Busemann flowfield is given in Figure 1. Air is captured by the inlet and compressed isentropically by a conical flowfield. The inlet flow then passes through an oblique shock at the throat, which reorients the flow to be parallel with the isolator. While this is a very efficient compression flowfield, its excessive overall length poses structural, drag, machinability, and heat transfer concerns [7]. Therefore, the inlet must be truncated, which reduces stagnation pressure recovery but dramatically reduces its length. Simply truncating the inlet at a certain point will result in a curved leading edge shock, which negatively impacts the downstream flow and results in a non-uniform inlet exit flowfield [8]. Therefore it is desirable to have a straight leading edge shock. Mölder addressed this issue with the conical flowfield designated as internal conical flow A (ICFA) [6]. The ICFA contour can be stitched to the truncated Busemann inlet to create a base flowfield, termed ICFC, that is highly efficient while retaining excellent flow uniformity.
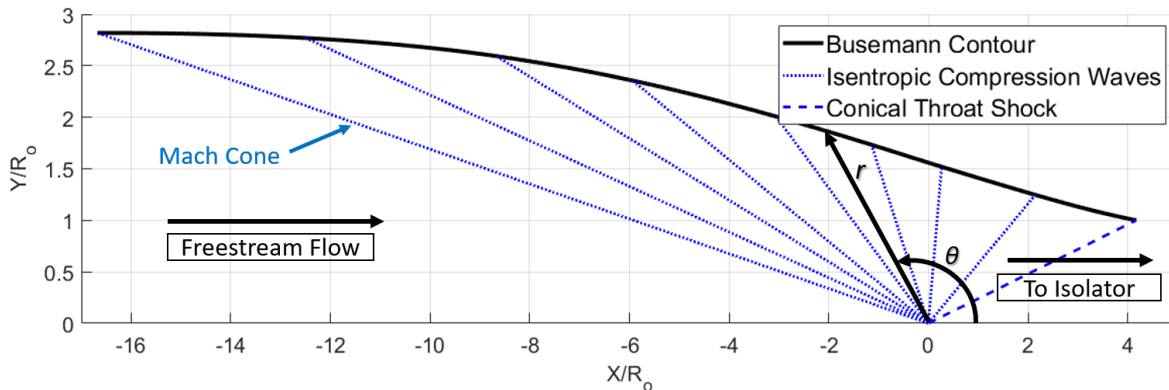

Fig. 1   Diagram of the classical Busemann flowfield described by Mölder [9].

While the ICFC is a highly efficient flowfield that is capable of satisfying all inlet requirements related to preparing the flow for combustion, it fails to allow for inlet starting for more than very mild compression ratios. Inlet unstart can be caused by many mechanisms; large vehicle attitudes, high back pressure, and high contraction ratios in the inlet are all common unstarting mechanisms [10]. For inlet design, an estimate for the starting contraction limit for the over-compression mechanism is given by the Kantrowitz Criterion [11]:

$$\left(\frac{A_e}{A_c} \right) = M_c \left[\frac{(\gamma+1)M_c^2}{(\gamma-1)M_c^2+2} \right]^{\frac{-\gamma}{\gamma-1}} \left[\frac{\gamma+1}{2\gamma M_c^2-(\gamma-1)} \right]^{\frac{-1}{\gamma-1}} \left[\frac{\gamma+1}{2+(\gamma-1)M_c^2} \right]^{\frac{\gamma+1}{2(\gamma-1)}} \tag{1}$$

where A_e is the exit area of the inlet, A_c is the capture area of the inlet, and M_c is the capture Mach number. For example, a weak throat shock in a high efficiency configuration operating at Mach 6, the Kantrowitz Criterion for the minimum inlet exit to capture ratio is 0.63. This, however, is considerably higher than the ratio given by the classical Busemann and ICFC style flow fields for any significant compression at high Mach numbers. Therefore, a technique has to be utilized to reduce the contraction of these highly efficient base flowfield types.

Streamtracing techniques have gained considerable attention as a method to design shape transitioned inlets. As an added benefit, streamline tracing techniques often provide ways to relieve the internal contraction ratio (ICR) of the original axisymmetric parent flowfields [3, 12]. During the design process, a capture shape and isolator exit shape are defined. If necessary, several intermediary shapes could be defined to enhance the shape transitioning process [2]. Thus, two or more streamlines from the parent flowfield are matched to follow the inner and outer radii. This creates an inlet which allows for mass spillage when operating off-design and a relieved ICR that satisfies starting conditions. The blending of streamlines is a fundamentally geometric technique that is a averaged combination of several different compression streamlines. This makes the final surface definition hard to analyze analytically and necessitates CFD and experimental verification of the resulting flow field.

The method of Osculating Axisymmetric Planes (OAP), developed by Sobieczky et al., allows designers to create complex three-dimensional wavecatcher inlet geometries based on multiple two-dimensional solutions of the chosen parent flowfield[13]. This method of streamtracing follows an aerodynamic transition by solving unique parent flowfields for each defined radial slice of an inlet. Historically, this method was applied to the design of high-speed waveriders [14]. Recently, however, the method of osculating planes was recently applied to the design of several three-dimensional, high-speed, and shape-transitioned inlets [15–18]. The advantages of this method include higher on-design mass capture, higher total pressure recovery, and finer control of the inlet's aerodynamic properties [16].

Viscous effects have a serious impact on the performance of a Busemann flowfield [19]. Viscous effects on shock angles, flow constriction due to boundary layer growth, and flow separation all can reduce the uniformity of inlet exit flow and drastically reduce efficiency, while increasing the chances of unstart. It is therefore imperative to account for viscous effects in the design of of an inlet. To offset the constriction and change in effective geometry by the presence of a boundary layer, a full viscous simulation of the inlet can be run, and the geometry offset by the local displacement thickness [20]. Flow separation, which is a product of adverse pressure gradients, should be minimized as much as possible. As shock waves create large adverse pressure gradients, it is critical to investigate flow separation at walls where the shock impingement occurs.

Building off of the work above, a code was developed to design custom self-starting inlets. The code creates mixed-contraction, high-speed inlet geometries by streamtracing unique solutions of the Busemann flowfield through a user-defined shape transitions. The theory of osculating axisymmetry is applied to stitch many local 2D flowfields together as an approximate design method for a 3D geometry. To create the compression surface, several iteration schemes work in-tandem to iterate on three key parameters: throat shock angle, throat Mach number, and centerbody radius. The outer loop was deactivated for expediency in the current project. The lower surface is then crafted through a local parallel-streamlines technique. All inlets are inward-turning by nature of the local Busemann flowfields. Table 1 shows the geometric design parameters for the finalized inlet. Additionally, the starting limits for the intake are presented in Figure 2. The design code incorporates a boundary layer viscous correction tool to adjust the inviscid surfaces outward by the estimated displacement thickness of a compressible turbulent boundary layer. Other blunting and export tools were also developed to ease model and mesh generation in CAD and CFD programs. Table 2 shows the analytical and CFD performance parameters for the inlet. More detailed description of the final geometry chosen for testing and the overall design process and CFD analysis can be found in Noftz et al., [21].

Table 1   User defined geometric inputs.

Geometric Parameter	Symbol	Value
Approximated Contraction Ratio	CR_{apr}	7
Inlet Aspect Ratio	AR_{in}	1
Isolator Aspect Ratio	AR_{iso}	2
Inlet Superellipse Exponent	n_{in}	2
Isolator Superellipse Exponent	n_{iso}	4
Isolator Height	h	1.8
Leading Edge Deflection Angle	δ	6°

Table 2   1D INlet performance parameters.

Flow Property	Symbol	Analytical	Inviscid CFD	Viscous CFD
Compression Ratio	P/P_∞	23.73	9.50	11.10
Total Pressure Recovery	$P'_\circ/P_\circ$	0.93	0.86	0.69
Cowl Mach Number	M_c	4.30	4.80	4.59
Throat Mach Number	M_3	3.38	4.09	3.60
Mass Capture Efficiency	$\dot{m}_{captured}/\dot{m}_{throat}$	1.00	0.83	0.80
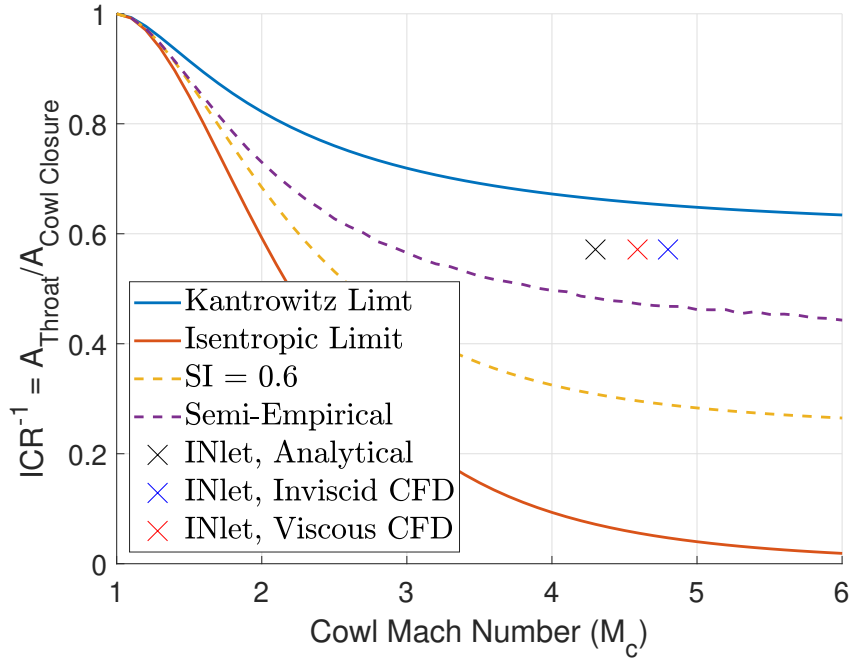
Fig. 2   Contraction limits of the INlet from analytical and CFD methods.

III. Facility and Model

A. Boeing-AFOSR Mach 6 Quiet Tunnel

Data was collected at Purdue University in the Boeing/AFOSR Mach-6 Quiet Tunnel (BAM6QT). The tunnel is a Ludwieg tube configuration, which was chosen to minimize cost while achieving fairly high freestream unit Reynolds numbers [22]. This design utilizes a long driver tube with heated air, followed by a converging-diverging nozzle that accelerates the flow to a nominal Mach 6 condition, and finally into a vacuum tank at the downstream end of the facility.

Through several design features the tunnel is capable of achieving quiet-flow freestream pressure fluctuations of less than 0.05% of the mean pressure [23]. The tunnel nozzle is polished to a mirror finish to inhibit roughness-induced boundary-layer transition. The boundary layer at the contraction exit is removed by a suction slot, ensuring a fresh, laminar one over the diverging portion of the nozzle [24]. This feature removes tunnel-wall boundary-layer disturbances that lead to a turbulent boundary layer in the diverging portion of the nozzle [23]. The bleed air bypasses the diverging nozzle and test section, feeding directly to the vacuum tank. The tunnel can be run under noisy-flow conditions by leaving a valve in the bleed piping closed, with noise levels on the order of 2.4 – 2.6% [23]. When the bleed line is open, quiet flow is achieved up to a maximum quiet stagnation pressure of 1 MPa [23].

Tests were nominally conducted at Mach 6.0 for quiet flow and Mach 5.8 for noisy flow (due to the thicker nozzle-wall boundary layer) [25], with both 0° and 6° angle of attack. The tests were conducted at a range of freestream unit Reynolds numbers with a maximum quiet Reynolds number of 13 x 10^6 / m.
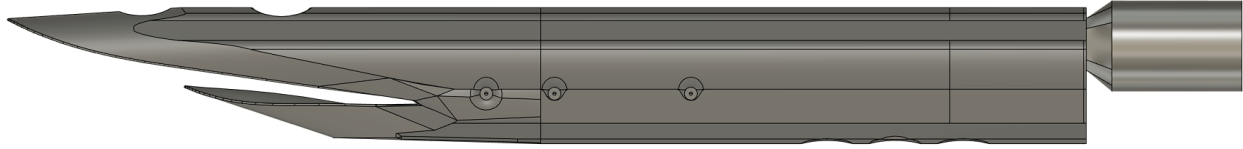
B. INlet Blockage Models

Wind tunnel starting is a complicated phenomenon that is not easily predicted through the use of experimental correlations or CFD. Although frontal area plays a significant role in determining total blockage, other factors like model pitch, non-conformal windows, boundary layer separation, boundary layer thickness, and SWBLI all play a role in determining tunnel startability [26]. To answer this question, two blockage models, based on a preliminary version of the Indiana Inlet design, were constructed for testing within the BAM6QT. These preliminary models have an over-sized lower lip surface, so pressure measurements and performance may deviate from the finalized model due to geometry changes. The smallest INlet model was scaled similarly to the 9% HIFiRE-6 202E model. This HiFIRE-6 model, on loan from the Air Force Research Laboratory, had previously undergone testing within the BAM6QT. Results showed that the BAM6QT successfully started with the model pitched at a variety of angles of attack and different freestream Reynolds numbers. A larger INlet version, dubbed "Medium Inlet," was scaled to a 14% HIFiRE-6 202E size and used to test the limits of tunnel starting.

These preliminary models were constructed without a boundary layer correction to the inlet's upper surface contour. The low momentum fluid in a boundary layer effectively shrinks the core flow area of the captured streamtube at the inlet's throat, artificially increasing the internal contraction ratio. Sufficient boundary layer growth may lead to flow over-contraction, potentially causing unstart [26]. To mitigate this phenomenon, the throat of the blockage models were enlarged to decrease the analytically defined internal contraction ratio. The throat was enlarged where the top compression surface connects with the isolator. It was enlarged by 0.20" for the 14% model and 0.10" for the 9% blockage model. Although enlarging the throat may cause off-nominal performance, this modification was deemed necessary to effectively study self-starting characteristics of the inlet until a full viscous correction could be developed and validated.

The two blockage models were rapidly prototyped from TriModels Inc. with CE-221 Cyanate Ester as the chosen material. The material's high heat deflection temperature and comparable strength to polycarbonate made it an attractive option for a blockage model [27]. Additionally, the digital light synthesis process was able to provide good resolution on leading edges and contours without producing any stair-stepping that is innate to fused deposition modeling. Unfortunately, the baking process produced stress cracks in both models. After a finite element analysis review, it was deemed necessary to reinforce these models. To reduce the risk of failure during a worst-case asymmetric tunnel unstart scenario, a compressive steel sleeve was wrapped around the inlet-isolator junction. Hose clamps were used to compress the sleeve around the body. In the event of failure, the sleeve would catch and hold the model together. Additional internal support rods were also drilled into the smaller model to alleviate bending stresses on the forward-most portions of the inlet surface. A figure showing a CAD rendering of the 14% scale blockage model is showed in Figure 3a.

Both blockage models were designed with eight access ports for Kulite pressure transducers. These ports were dispersed throughout the internal flowpath of the model to give indicators on inlet operation. The location of these sensors were constrained due to the internal support rods. Thus, there are sensors placed on the sidewall, top, and lower

portion of the IML. A back-pressure blowing port was also located within the isolator. This quick-disconnect blowing port makes it easy to conduct forced-unstart experiments and compare started against unstarted inner flow paths. The locations of the Kulites within the blockage models are shown in Figure 3b for reference. Dashed-red lines delineate the different regions of the model, which include the external contraction, internal contraction, rectangular isolator, and blended nozzle.

(a) CAD of the 14% scaled blockage model.
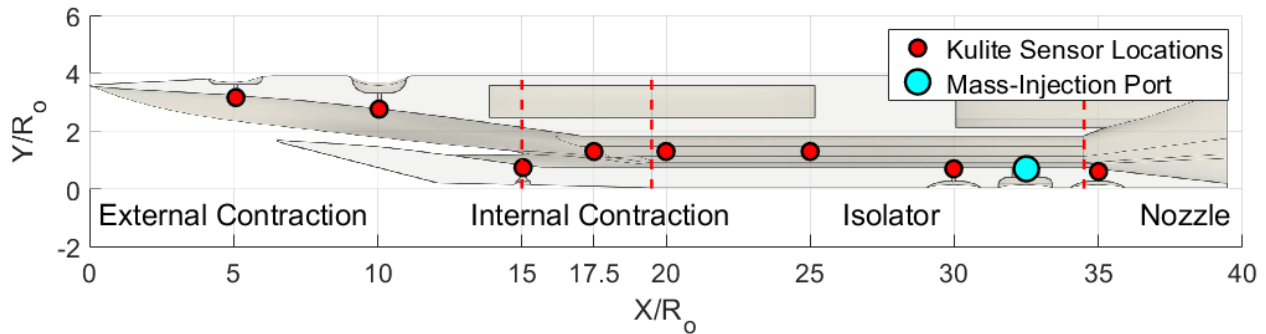
(b) Normalized sensor locations of the designed blockage models.

Fig. 3   Schematic and sensor locations of the INlet blockage models.

IV. Blockage Test Campaign

The blockage test campaign was designed to test the limits of tunnel starting and the self-starting ability of the INlet blockage models. The two models were run at various freestream Reynolds numbers, sting positions, one non-zero angle-of-attack, under quiet flow, and under noisy flow. Due to the compromised structural integrity of the models from internal cracks, it was deemed too risky to attempt schlieren visualization. As a precautionary measure, the wind tunnel sapphire windows were replaced with stainless steel blank inserts. Fortunately, both models survived installation and testing without failing.

A. Tunnel Starting Analysis

Wind tunnel starting is hard to predict for irregularly shaped geometries. Experimental correlations that apply to sharp and slender conical geometries may not apply to non-axisymmetric geometries like inlets. inlet models also contain an internal flowpath that may interact with the start-up processes of a wind tunnel. It is computationally expensive to grid and solve the flowfield for an entire wind tunnel system. Blockage models are a comparably cheaper and faster method to determine a suitable size for final testing. However, care must be taken to analyze tunnel behavior with blockage models.

1. Hot Film and Nozzle Wall Pressure Traces

Tunnel diagnostic sensors, such as the hot film (HF) and nozzle wall Kulite (NWK), provide a quantitative assessment of abnormal tunnel behavior. A sample case of tunnel unstart assessment is shown in Figures 4a and 4b for the 14% model under Mach 6 quiet flow with an initial burst stagnation pressure of 170.3 psia. The uncalibrated hotfilm voltage signal is shown in Figure 4a. The HF voltage fluctuations are computed by integrating power spectra from 0 kHz – 50 kHz for 0.1 second window increments over the length of the run. The nozzle wall pressure trace in Figure 4b is also

compared against isentropic freestream static pressure for Mach 6 and Mach 5.8 flow. The error between the real and expected wall pressures from 0.25 – 3.5 seconds is calculated. This array of values is then averaged together to find the average deviation of the nozzle wall pressure trace from the expected isentropic behavior. This range of time was selected to avoid start-up and shut-down behavior.

The nozzle wall pressure trace shows start-up behavior from 0 - 0.25 seconds into the run. The establishment of quiet flow occurs at 0.5 seconds and lasts until 3 seconds. A mid-tunnel unstart is observed in both the HF and NWK plots at 1.5 seconds into the run and lasts 0.25 seconds. This is likely due to nozzle wall boundary layer separating and then reattaching. After this event, the tunnel stays started until the 3.8 seconds mark. However, HF RMS calculations show a noticeable increase in noise starting 2.8 seconds after establishment of quiet flow. This is consistent with the "2-second rule" described by Mamrol's tunnel characterization study [28]. Additional care must be taken when analyzing nozzle wall pressures. Sometimes the recorded static pressure will not match the static pressures predicted by isentropic theory for a Mach 6 freestream. Juliano showed from pitot measurements that separation events would cause the freestream flow to drop as low as Mach 5 with initial stagnation pressures as low as 45 psia [29].

2. Reynolds Number Starting Maps

The nozzle wall pressure traces for several different tunnel runs over a Reynolds sweep can be compiled together to provide a better understanding of tunnel startability. These "Starting Maps" show abnormal behavior in the nozzle wall pressures as a function of freestream Reynolds number. Two maps are presented in this section for the medium 14% scale blockage model. The medium blockage model had worse overall starting performance than the 9% blockage model.

The first starting map in Figure 5a is for the 14% model at 0° AoA under Mach 6 quiet flow. Five tunnel runs were conducted at various starting stagnation pressures. Vacuum tank pressures were recorded to be under 15 torr for each run. The 170.1 psia (1.17 MPa) and 130.5 psia (900 kPa) runs show a momentary mid-tunnel unstart occurring due to nozzle wall boundary layer separation. The flow cannot be considered Mach 6 steady-state during these unstart events. This stresses the importance of a tunnel starting analysis preceding model data analysis. Additionally, sustained tunnel unstart is seen for the tunnel runs below a starting 86.1 psia (594 kPa) stagnation pressure. The average deviation of the theoretical isentropic pressures and the measured pressures are above 70% for these cases.

The second starting map shows the 14% model under similar tunnel conditions at 6° AoA. Figure 5b shows the Reynolds sweep conducted for this orientation. The 130.5 psia (900 kPa) run shows a momentary mid-tunnel unstart occurring due to nozzle wall boundary layer separation. Additionally, sustained tunnel unstart is seen for the tunnel runs below a starting 60.2 psia (415 kPa) stagnation pressure. The average deviation of the theoretical isentropic pressures and the measured pressures are above 70% for these cases.

The results of these "Starting Maps" show that the tunnel starts consistently across all Reynolds numbers tested for the 9% model for Mach 6 quiet flow. The 14% scale model appears to unstart the tunnel at freestream Reynolds numbers below $8 \cdot 10^6/m$. Interestingly, tunnel starting issues disappear completely for noisy flow conditions at all Reynolds numbers tested. The results of the tunnel starting analysis influenced the scaling of the final inlet model, which was based on a 12% scale. This was determined to be the best compromise between model length, structural strength, viewing area, and tunnel startability.
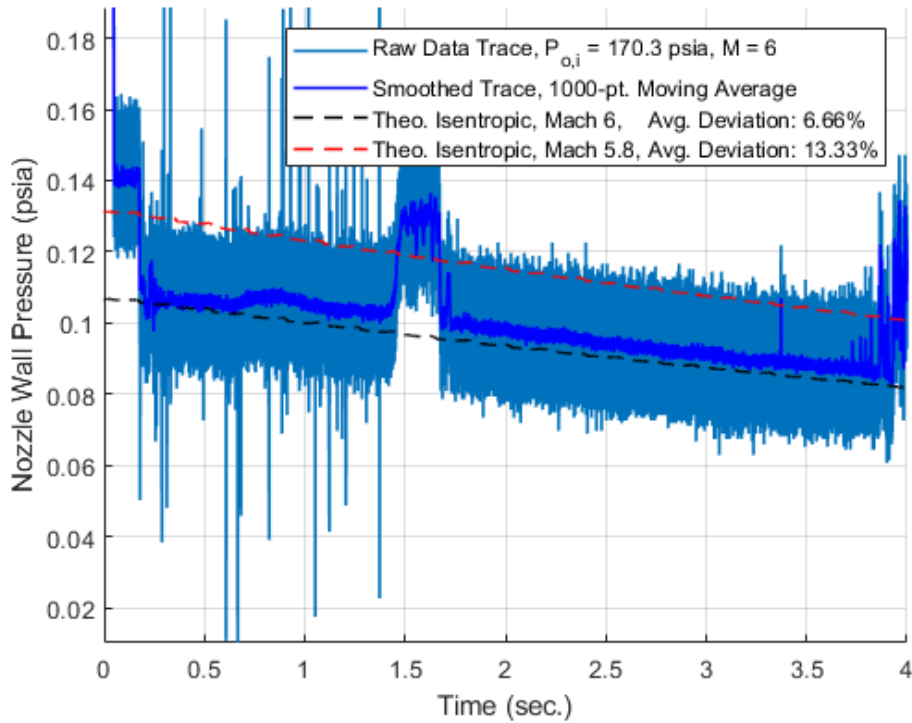
B. Inlet Starting Analysis

The second objective of the test campaign was to conduct a preliminary study on the self-starting characteristics of the INlet blockage models. The blockage models were designed with an over-sized lower lip because of an error in the streamtracing code. Due to this deviation from the target geometry, the experimental results cannot be directly compared to the benchmarked CFD results. Also, there were tunnel starting difficulties at low freestream Reynolds numbers ($Re_m < 8.0 \cdot 10^6/m$) for the 14% scaled blockage model, so only data from Reynolds number cases above this value are presented.

Inlets are designed to compress freestream flow for downstream components in an air breathing engine. For a scramjet, the establishment of supersonic flow in the isolator is essential. Determining the state of the ingested flow can be determined through static pressure measurements. Initial analysis of the inlets was accomplished by calculating the mean flow pressures along the IML Kulite sensors for verified started tunnel conditions. The mean pressures were calculated over 200,000 points (0.1 seconds) of data centered around the targeted Reynolds number condition. These results were then normalized by the theoretical freestream static pressure predicted by isentropic theory.
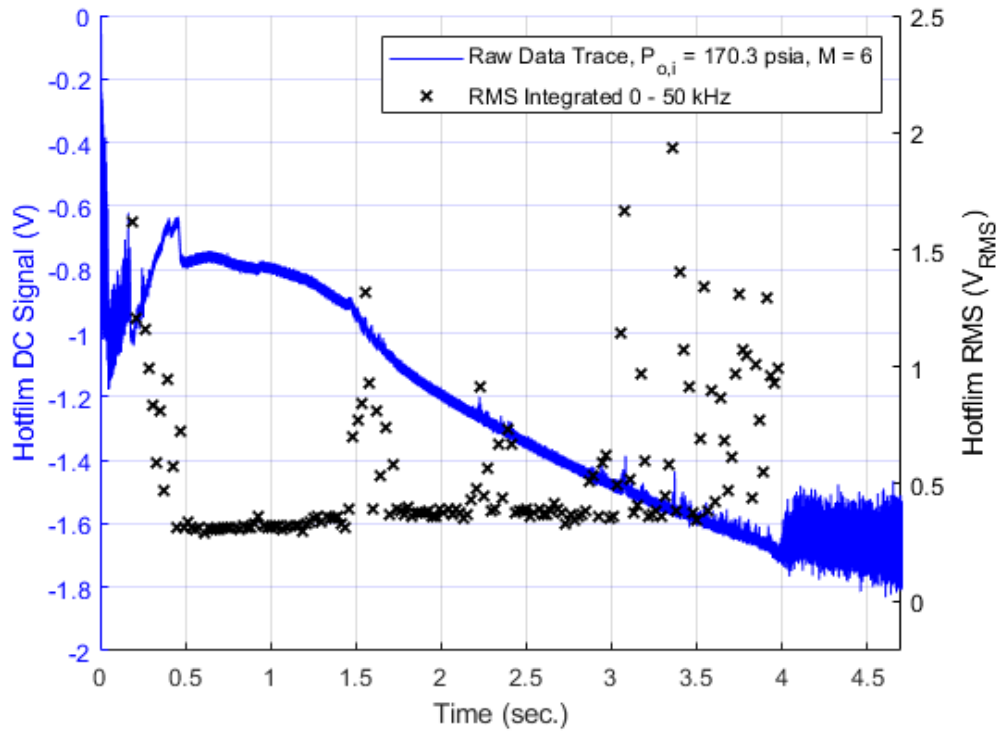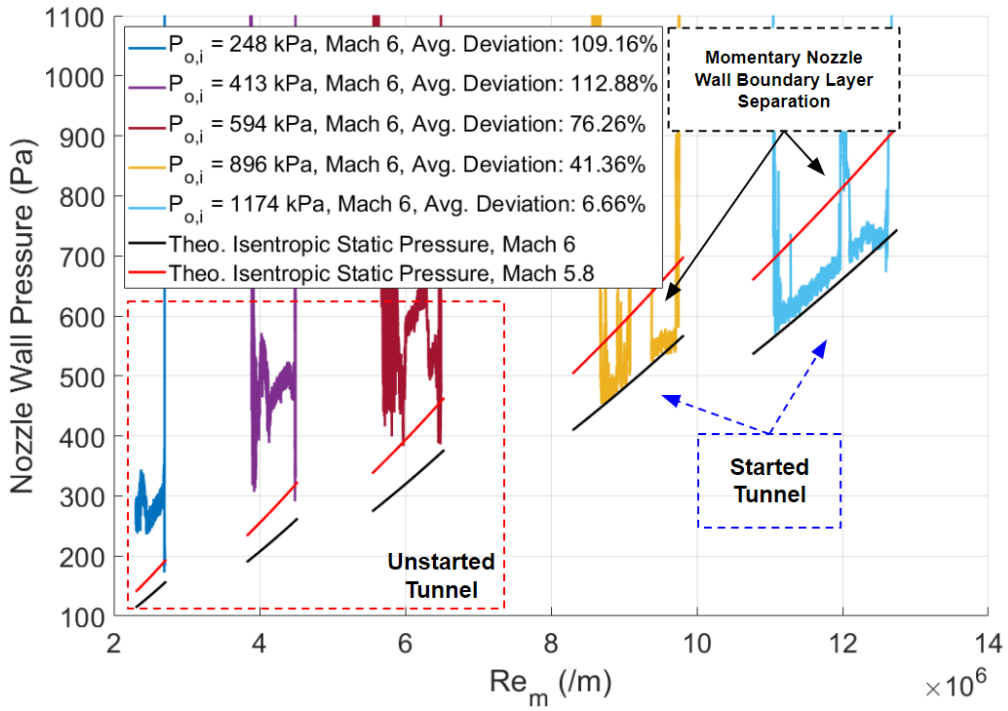
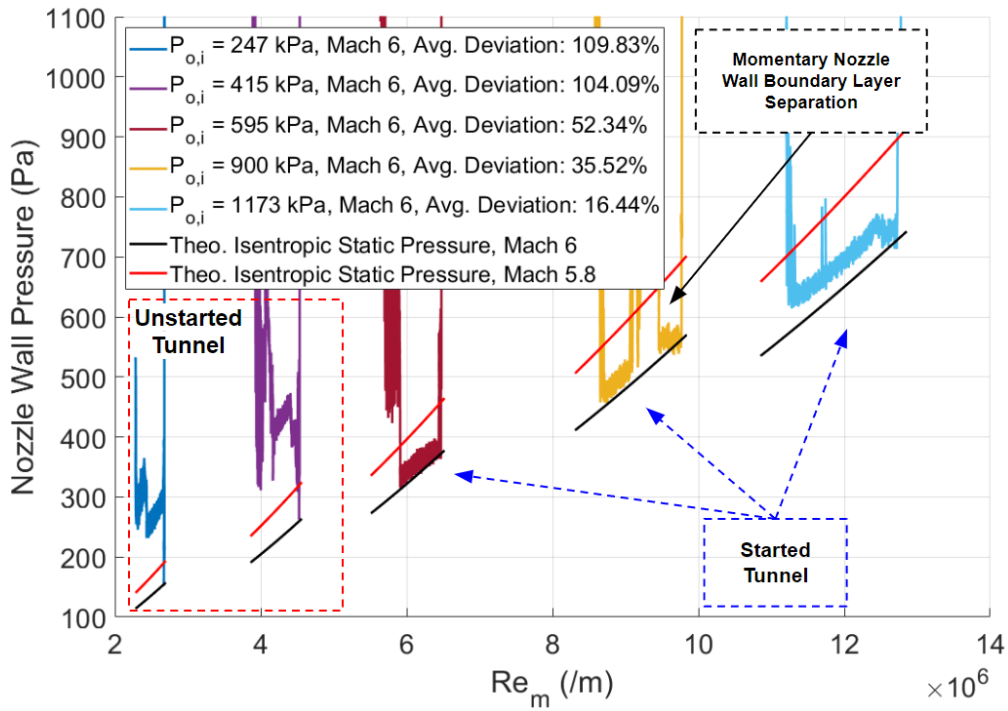(a) Hot film DC signal and fluctuations for a BAM6QT run.

(b) Nozzle wall pressure compared with isentropic theory.

Fig. 4   Tunnel starting analysis for the 14% model at $0°$ **AoA,** $P_{\circ,i} = 160$ **psia, and Mach 6 quiet flow.**

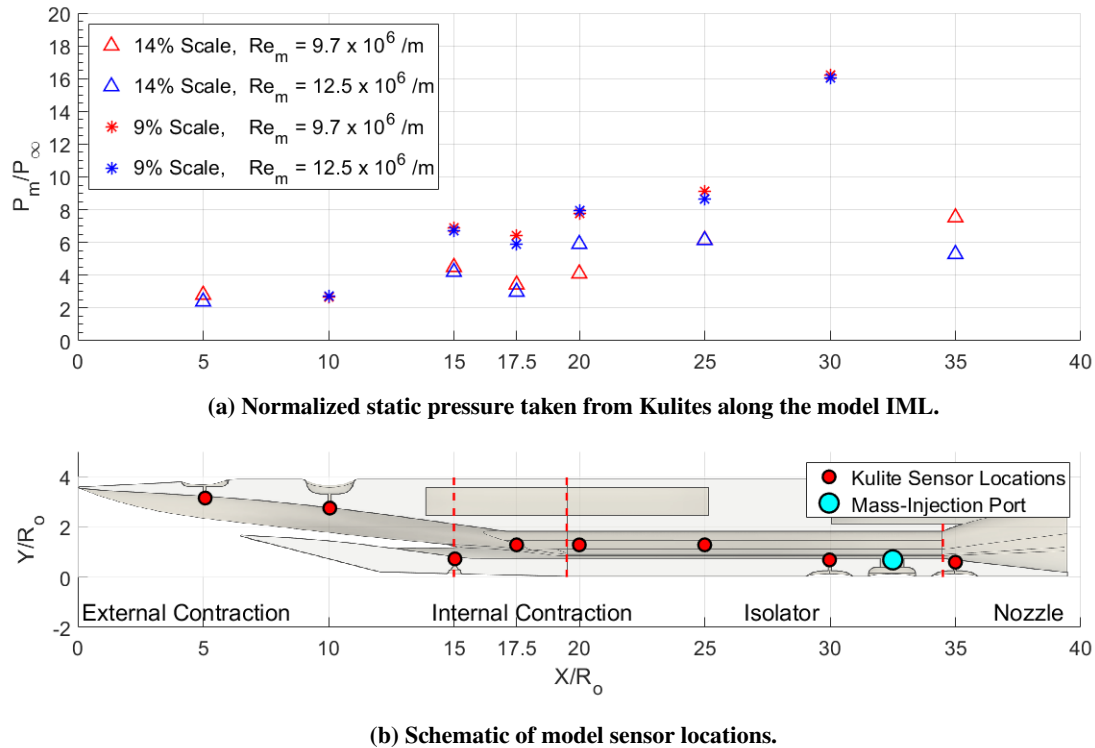**(a)** Wind tunnel starting map with INlet pitched at $0°$ AoA.

(b) Wind tunnel starting map with INlet pitched at $6°$ AoA.

Fig. 5   Wind tunnel starting maps for the 14% scale INlet blockage model at Mach 6.

1. Pressure Profiles

Internal flowpath static pressures were recorded from Kulite pressure transducers. The Kulite at $X/R_o = 15$ is located directly at the cowl plane, which is where incoming flow can spill overboard. During inlet unstart, a normal shock will take position at the beginning of the internal contraction, making this Kulite important for determining a started inlet state. Also, the Kulite at $X/R_o = 20$ is located directly nearby the throat, which is defined at $X/R_o = 19.5$ for all geometries. Depending on the model, some Kulites were excluded from the analysis due to abnormal readings or breaking during the entry. A variety of different conditions were compared with each other to determine the startability of the INlet models. Although two separate sting positions were tested, results from the sting-forward position are omitted from this analysis. The effect of sting position is negligible for a started tunnel that is operating in Mach 5.8 noisy flow or Mach 6 quiet flow. This is expected since the Mach 6 core flow should not be influenced by the sting position for a successfully started tunnel.

The effect of model scale on internal pressures is shown in Figure 6a. Model scale had a substantial effect on internal pressures past the $X/R_o = 15$ location. Pressure ratios downstream of this location were higher for the smaller 9% blockage model across two separate Reynolds numbers. It is likely the smaller model had less relative on-design spillage than the larger model, allowing for more efficient compression. The over-sized lower lip on the 14% model may also have had a more drastic effect on shock structure and flow spillage. Additionally, normalized pressures for both models appear independent of Reynolds number.

(a) Normalized static pressure taken from Kulites along the model IML.

(b) Schematic of model sensor locations.

Fig. 6   Model scale and freestream Reynolds number comparison for a Mach 6 quiet flow condition at 0° AoA.

The internal pressure profiles also reveal other trends about the inlet model. There appears to be a consistent drop in pressure gain at the $X/R_o = 17.5$ sidewall Kulite location across several different conditions. This loss in pressure may be related to the on-design spillage phenomena discussed in previous sections. If flow is being spilled, then the high-pressure air is leaving the inlet and dropping the static pressure. Future schlieren studies will confirm this result and its affect on the leading shock structure. The Kulite pressure transducers in the inlet's isolator section also measure a gradual rise in static pressure. This is likely due to the isolator shock-train, which causes additional pressure gain to the captured flow.

For a functioning high-speed inlet, the incoming flow must be compressed and remain supersonic. The pressure

profiles reported here show consistent trend of increasing mean pressure throughout the streamtube flowpath. Subsonic pressures past the throat region are indicative of an unstarted inlet and are calculated based on the 1D normal shock equations. Normal shock pressure ratios are on the order of $P_{i+1}/P_i \approx 10.3$ at Mach 3 and $P_{i+1}/P_i \approx 18.5$ for Mach 4. These ratios must be multiplied by the pressure gain ratios through the leading oblique shock for Mach 6 flow at a 6° deflection angle ($P_i/P_\infty \approx 2.3$) and the isentropic compression from the inlet's inward-turning surface. If the isentropic pressure gain is neglected, the final throat pressure ratios would be $P_m/P_\infty \approx 23.7$ and $P_m/P_\infty \approx 42.5$, for a Mach 3 and Mach 4 throat, respectively. The reported values are sufficiently below this margin, with the highest throat pressure ratio nearing $P_m/P_\infty \approx 8$ for the small inlet case. It is safe to assume, with these calculations, that the inlet has successfully self-started for all reported conditions and is compressing the captured streamtube.

C. Inlet Mass-Injection

The resistance of inlet systems to forced unstart is an important quantity that provides a safe operating margin for flight vehicles. Unstart can be simulated by choking the flow within the isolator through several different mechanisms. A mechanical blockage, such as a downstream conical plug, provides throttling capability if the plug is moved into the isolator and restricts the core flow's exit area. A thermal blockage occurs from combustion that drives the flow to a sonic condition from the Rayleigh flow condition. Also, the flow can be choked from mass-injection. This last method was used in the experiment to simulate a back-pressure condition at different freestream Reynolds numbers. The amount of flow injected into the isolator was calculated by assuming choked exit flow at the isolator's injection port. The choked flow relation for a perfect gas is shown in equation (2), where P_t and T_t are stagnation pressure and temperature of the plenum gas.

$$\dot{m}_{injection} = A_{orifice} P_t \sqrt{\frac{\gamma}{RT_t}} \left(\frac{\gamma + 1}{2} \right)^{-\frac{\gamma+1}{2(\gamma-1)}} \tag{2}$$

The jet-injection system consisted of a plenum of high-pressure air that is routed into the blockage models through a nylon tube. The stagnation pressure of the plenum (P_t) was set to a constant of 30 psig for all mass-injection studies. Total temperature of the air was taken as room temperature ($T_t = 293K$). Due to time limitations, the mass-injection studies were only performed on the small 9% scale blockage model. The injection system was triggered approximately 0.75 seconds after the fast-valve was activated. The delay ensures that the tunnel can sufficiently start and gives a small window to collect reference data before the mass injection begins.
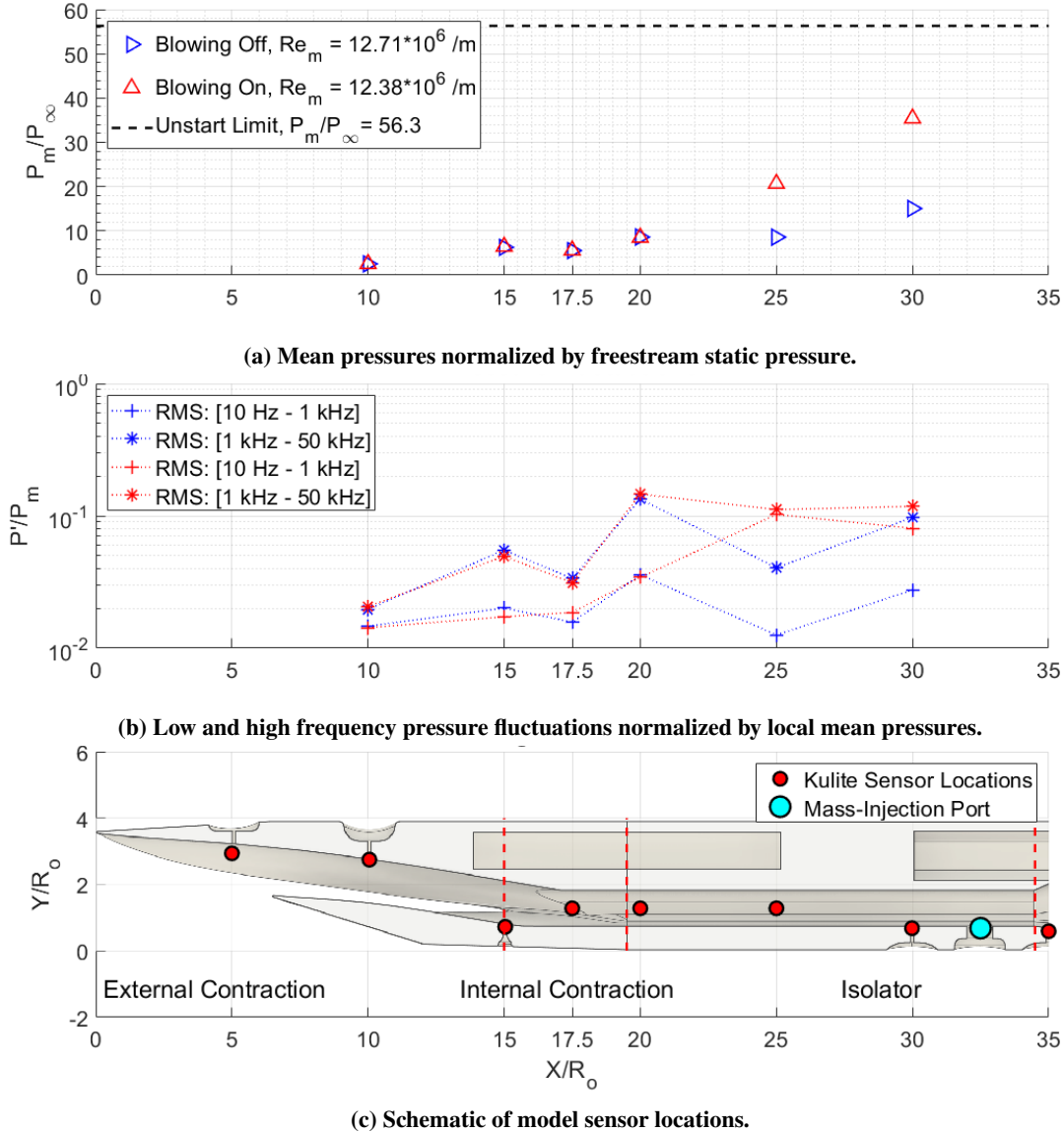
1. Back-Pressure Profiles

The back-pressure study was conducted with the 9% model at 0° AoA for three freestream Reynolds numbers ($Re_m = 12.7 \cdot 10^6/m$, $Re_m = 9.7 \cdot 10^6/m$, $Re_m = 6.4 \cdot 10^6/m$) which are referred to as the high Reynolds number, medium Reynolds number, and low Reynolds number condition, respectively. All back-pressure runs were conducted at a Mach 6 quiet flow condition. The state of the internal flow path was determined through mean pressure and pressure fluctuation measurements. Mean pressures were calculated from the averaged DC pressure signal trace for a 0.1 second (200,000 point) increment. Pressure fluctuations were calculated by integrating the power spectra of the 0.1 second sampled signal over a given frequency range. A low frequency band [10 Hz - 1 kHz] and a high frequency band [1 kHz - 50 kHz] was defined. The power spectra was integrated over these frequency bands to find the band-limited RMS fluctuation magnitude. These pressure fluctuation values were normalized by the mean pressures for their respective location. Two states of the inlet are compared at each freestream Reynolds number condition: mass-injection active (Blowing On [Red]) or no mass-injection (Blowing Off [Blue]).

It is helpful to have a rule-of-thumb for the estimated pressure rise within the internal contraction during inlet unstart. A series of 1D pressure ratios can be solved from theoretical calculations to give this estimate. It is known that the leading oblique shock is turned by a 6° wedge angle for all osculating plane solutions. The leading shock pressure ratio is calculated as $P_i/P_\infty = 2.3$ from the oblique shock relations. Viscous CFD shows that the captured streamtube is at Mach 4.6 at the beginning of the internal contraction. If a standing normal shock develops there, then the pressure rise estimate is $P_{Throat}/P_i = 24.5$ from normal shock relations. If intermediate isentropic compression from the inlet surface is neglected, then the total pressure ratio is $P_{Throat}/P_\infty = 56.3$ for an unstarted inlet.

The highest Reynolds number case ($Re_m = 12.7 \cdot 10^6/m$) studied with the jet-injection system is presented in Figure 7. During the blowing event, the maximum back-pressure ratio in the isolator reaches $P_m/P_{inf} \approx 36$. The effect is immediately noticeable when compared to the baseline blowing-off condition at locations $X/R_\circ = 25$ and

$X/R_\circ = 30$. No other upstream influence appears on sensors. Although the isolator shock train moves forward, the back-pressure is not strong enough to eject it from the inlet. Interestingly, low frequency RMS content appear to dominate the unsteadiness measurements at $X/R_\circ = 25$ and $X/R_\circ = 30$ compared to pre-blowing data. Elevation in low frequency content is likely due to shock unsteadiness, which suggests shock train movement from the blowing event. RMS fluctuations upstream of $X/R_\circ = 25$ appear similar to pre-blowing data.

(a) Mean pressures normalized by freestream static pressure.

(b) Low and high frequency pressure fluctuations normalized by local mean pressures.
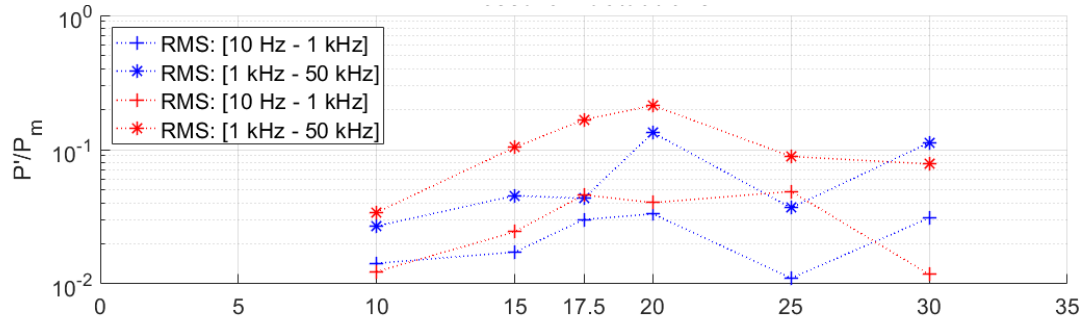

(c) Schematic of model sensor locations.

Fig. 7 INlet flowpath analysis at $Re_m = 12.7 \cdot 10^6/m$ before and during back-pressure blowing.

The second highest Reynolds number run ($Re_m = 9.7 \cdot 10^6/m$) is shown in Figure 8. The effect of blowing is immediately apparent from the rise in isolator pressure ratios. The pressure transducers at $X/R_\circ = 25$ and $X/R_\circ = 30$ show a jump to $P_m/P_{inf} \approx 60$. However, the throat pressure transducer at $X/R_\circ = 20$ stays below the predicted throat unstart pressure ratio of $P_{Throat}/P_\infty = 56.3$. The isolator shock train has not yet been disgorged from the inlet and the inlet remains fully started. However, increases in pressure at the $X/R_\circ = 15$ and 17.5 locations hint at change in the throat shock strength.

Analysis of the RMS pressures show an elevation of the high frequency and low frequency content above baseline at nearly all locations. One exception is the last sensor location at $X/R_\circ = 30$, which is directly ahead of the mass-injection port. Fluctuations also appear to affect the sensor at $X/R_\circ = 10$. This sensor is in the external contraction of the inlet,
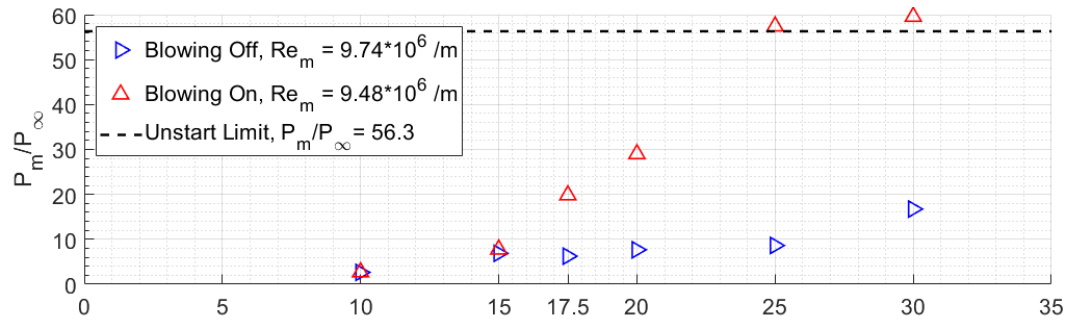
(a) Mean pressures normalized by freestream static pressure.

(b) Low and high frequency pressure fluctuations normalized by local mean pressures.
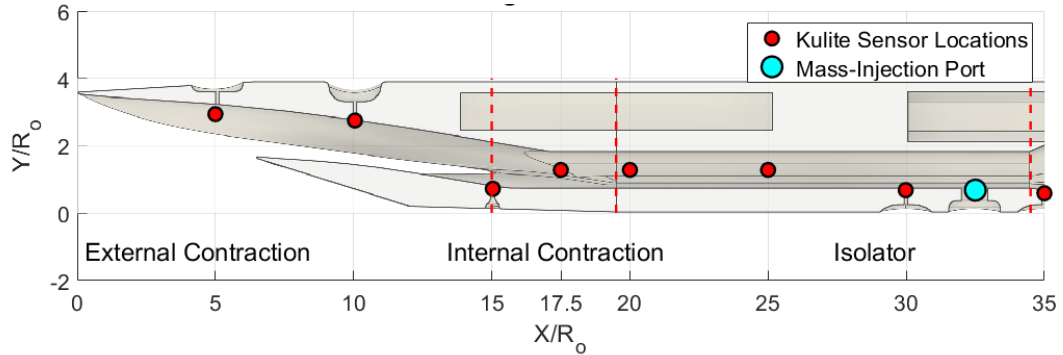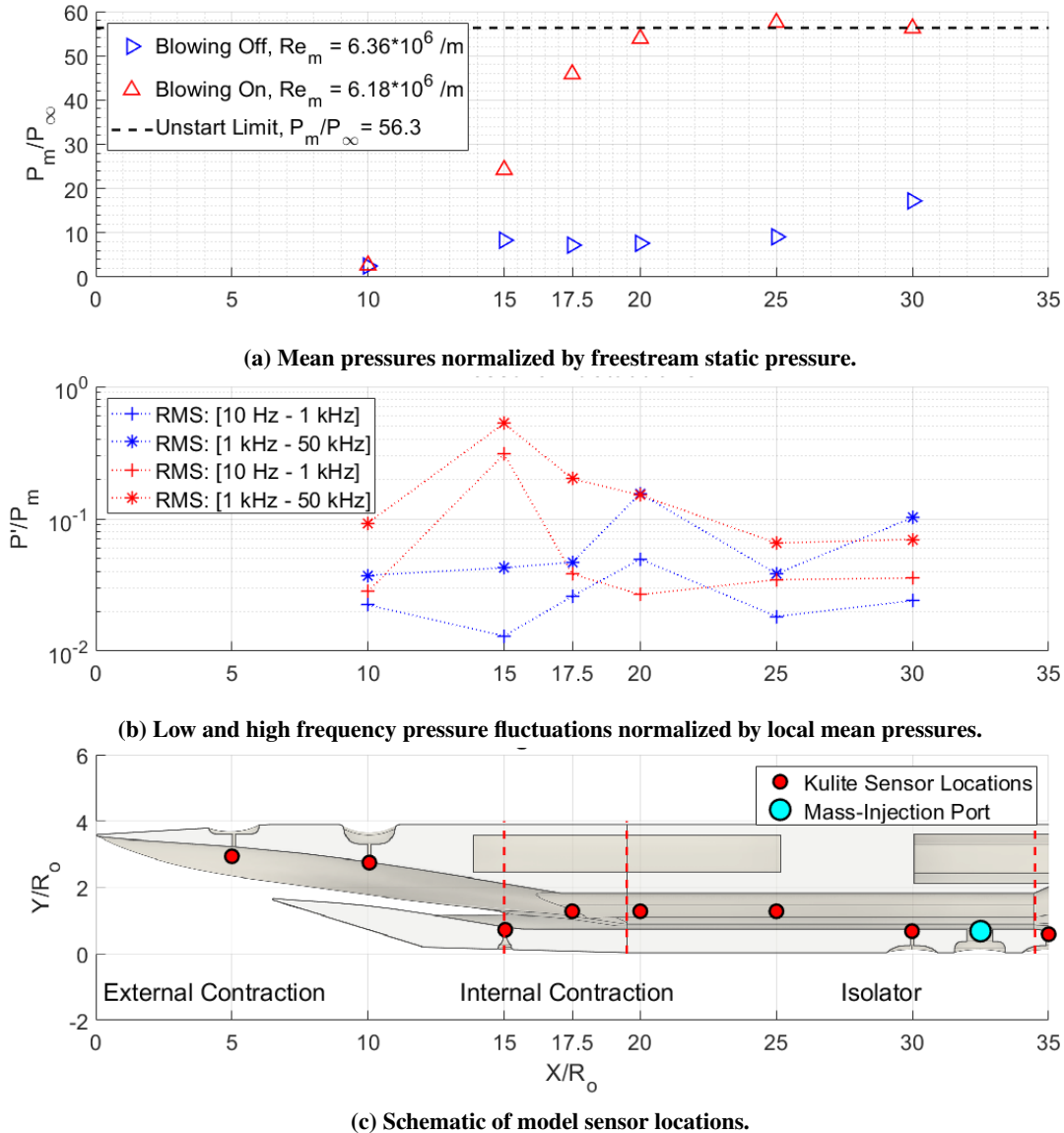

(c) Schematic of model sensor locations.

Fig. 8   INlet flowpath analysis at $Re_m = 9.7 \cdot 10^6/m$ before and during back-pressure blowing.

so any perturbations would have to travel upstream through the boundary layer. Downstream changes in a scramjet isolator can travel upstream, even if the inlet remains fully started.

The last jet-injection run was conducted at $Re_m = 6.4 \cdot 10^6/m$ and presented in Figure 9. This final case shows the most drastic changes in internal mean pressures and RMS pressures. In this case, the back-pressure resistance appears to flatten at $P_m/P_\infty \approx 60$ for most sensors within the isolator. The throat unstart pressure limit ($P_{Throat}/P_\infty = 56.3$) is nearly surpassed. The isolator shock has propagated upstream and is likely disgorged from the inlet at $X/R_o = 15$, which is the start of the internal contraction. A soft inlet unstart is witnessed with likely flow spillage in along the cowl notches.


(a) Mean pressures normalized by freestream static pressure.

(b) Low and high frequency pressure fluctuations normalized by local mean pressures.

(c) Schematic of model sensor locations.

Fig. 9 **INlet flowpath analysis at $Re_m = 6.4 \cdot 10^6/m$ before and during back-pressure blowing.**

There is an elevation in RMS pressures for all locations except for $X/R_o = 30$. The most drastic spike in RMS is seen at $X/R_o = 15$, where the blowing-on values are nearly two orders of magnitude larger than baseline. This is likely due to an unstable normal shock sitting in this region, causing unsteady flow spillage. Similar to the medium Reynolds case, fluctuations are traveling upstream and effecting RMS values at the $X/R_o = 10$ location. The power spectra of the Kulites during this specifc back-pressure event are analyzed in section IV.C.5.

14

2. Shock Arrival Tracking

A shock tracking code was developed to determine the speed of the leading shock in the isolator shock train during back-pressure and unstart events. The DC pressure signal from Kulites along the inlet's IML was used to calculate the isolator's shock movement over time. A moving-average of 40,000 points (0.02 second increments) of the DC pressure signal was computed to show large changes in static pressure. Additionally, three separate methods were used to calculate pressure fluctuations. The first two methods calculate mean-removed RMS pressure fluctuations over 0.02 second window increments for specific frequency bands. A low frequency band [50 Hz - 5 kHz] and a high frequency band [50 Hz - 50 kHz] was defined. The power-spectra was integrated over these frequency bands to find the total RMS fluctuation magnitude. The PSDs were calculated from Welch's method with 50% window overlap and a frequency resolution of 100 Hz. A third method calculated mean-removed standard deviation of the same signal. All methods were calculated over a trailing 0.02 second window to simulate real-world detection. Pressure RMS and STD values were normalized by the mean pressure over the same time window.

It was determined that the standard deviation calculations show the clearest distinction of shock pass-over during analysis. A comparison of the three methods is provided in Figure 10. RMS calculations show changes from shock pass-over, but peaks are not as prominent and sometimes do not appear at all. Prominent, consistent peaks are required to for the Matlab peak-finding function to automatically detect the shock. The peak-finding function is fed the array of standard-deviation values for a given sensor and discriminates peaks that are larger than 3x the standard deviation of the data. The peak is located, recorded, and plotted.
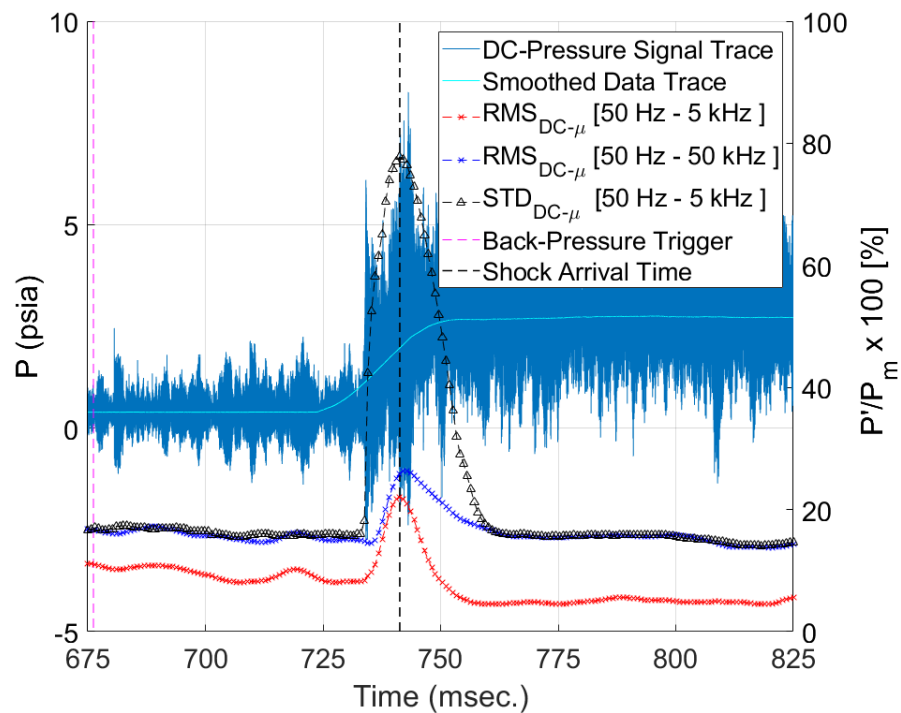
Fig. 10 Shock arrival detection example for the INlet unstart case at $Re_m = 6.4 \cdot 10^6/m$ for Kulite at $X/R_\circ = 20$.

The standard deviation values of for each sensor are shown in Figure 11. The plot clearly shows the shock traveling upstream in time. The shock speed also fluctuates. It moves quickly through the isolator, but slows down as it nears the internal contraction. Since time between peaks and distance between sensor locations are known, the average speed of the ejected shock can be calculated later. Although sensors at $X/R_\circ = 10$ and 15 do not see a shock, they do see elevated deviation values. Information from the back-pressure event has propagated upstream past the standing shock that sits in the cowl plane at the start of the internal contraction.
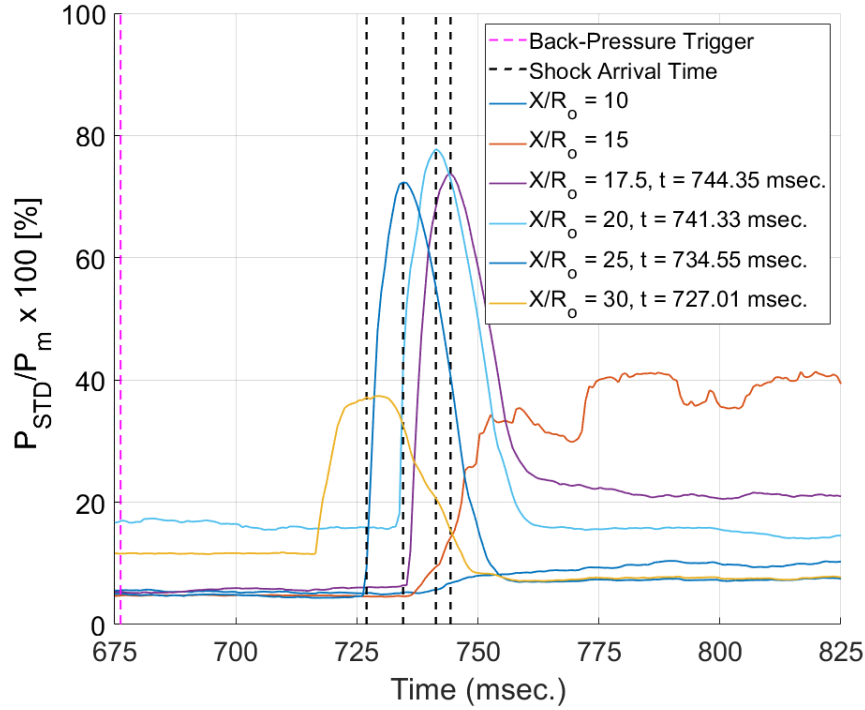
Fig. 11   Normalized standard-deviation calculations from the INlet back-pressure case at $Re_m = 6.4 \cdot 10^6/m$.

3. Unstart Detection

Although the initial jet plenum stagnation pressure was equivalent between runs ($P_t = 30$ psig), the speed of the shock train was not. There is a general trend of faster shock-train movement at lower freestream Reynolds numbers. Two potential effects are acting to change the speed of the isolator shock train. The first effect is the thickness of the boundary layer. A thicker boundary layer, from a lower freestream Reynolds number, may restrict the core flow area at the throat. This constriction decreases the isolator Mach number and makes it more susceptible to inlet unstart. The second effect is that the total massflow ingested by the inlet drops with lower freestream Reynolds numbers. The maximum ingested massflow of the inlet is analytically calculated by assuming 100% freestream capture of the incoming streamtube. Equation (3) gives the relation for massflow rate in terms of Mach number (M), static pressure (P_s), and static temperature (T_s). These terms are known from the freestream tunnel conditions. A lower tunnel stagnation pressure necessarily means a lower massflow rate through the tunnel core flow and the inlet.

$$\dot{m}_{Capture_{Analytical}} = \frac{P_s}{RT_s} A_{frontal} M \sqrt{\gamma RT_s} \tag{3}$$

The theoretical massflow capture estimate can be compared to a reference CFD calculation. The CFD massflow rate is calculated by taking area-averaged quantities of density (ρ_{avg}) and axial velocity ($v_{x_{avg}}$) at the throat. The CFD throat area is scaled to match the 9% blockage model size. The full relation is shown in equation (4). The CFD solution accounts for upstream overboard mass spillage, so it will be lower than the perfect-capture estimate of the analytical prediction.

$$\dot{m}_{Capture_{CFD}} = \rho_{avg} A_{throat} v_{x_{avg}} \tag{4}$$

Since the amount of massflow injected in the isolator is constant throughout the jet-injection study, the only variable that changes drastically is the incoming massflow rate determined by tunnel conditions. If the ratio between the captured massflow rate and the injected massflow rate is taken as a function of shock speed, a clear trend emerges. Figure 12 shows that faster shock speeds occur from larger massflow rate fractions. This makes sense intuitively because there is less upstream mass and momentum to slow the forward-moving shock train. If the massflow fraction becomes too large, then the inlet-isolator system cannot accept any more air before choking. The shock train is disgorged and unstart

16

occurs. The error bars in the plot represent the slowest and fastest shock speeds measured from the shock-tracking code. The average of all calculated shock speeds is the centered data point.
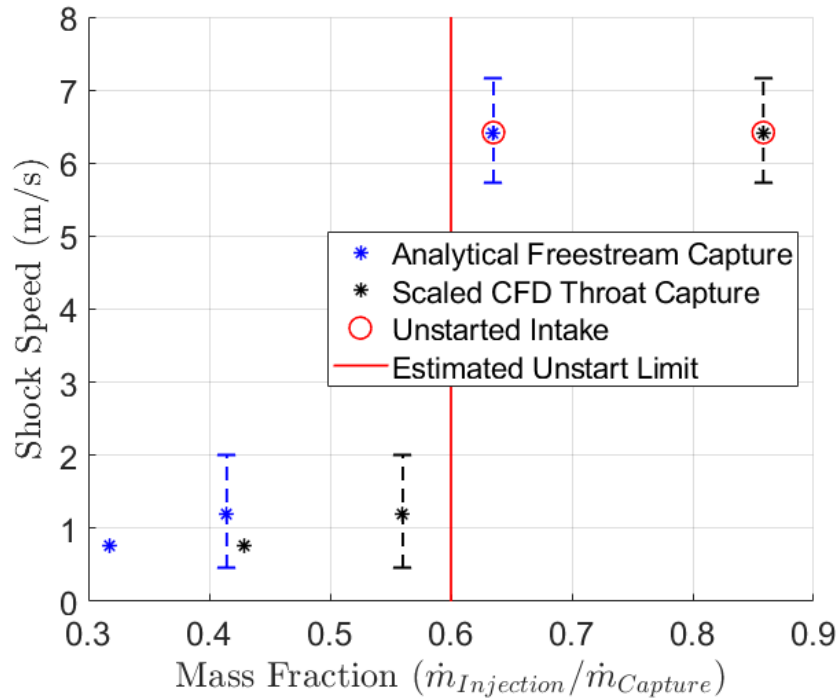

Fig. 12   Shock speed as a function of massflow ratio with the estimated unstart limit.

4. Extrapolated Unstart Boundary

An unstart map for the 9% model can be constructed from two independent variables: tunnel stagnation pressure ($P_\circ$) and jet-injection plenum stagnation pressure (P_t). From these quantities, it is possible to determine the inlet massflow rate through equations (3) or (4). The injected massflow rate is similarly known from equation 2. The ratio of the captured massflow rate and injected massflow rate act as a dependent variable. Plotting these three variables against each other creates an operability map for the combined tunnel and inlet model system using the CFD captured mass flow rate from equation 4 (Figure 13).

The two-dimensional contour shows what combination of jet-injection mass flow rate and tunnel stagnation pressure is required to achieve a certain massflow fraction. If the massflow fraction is high enough, then the inlet will unstart. The estimated unstart limit is denoted by the red line that is equivalent to a massflow fraction of 60%. The map can be modified for larger models by adjusting inlet capture area values. The CFD massflow capture estimate is more accurate than the 100% theoretical capture estimate because it accounts for spillage. The CFD captured massflow estimate was used for this plot.
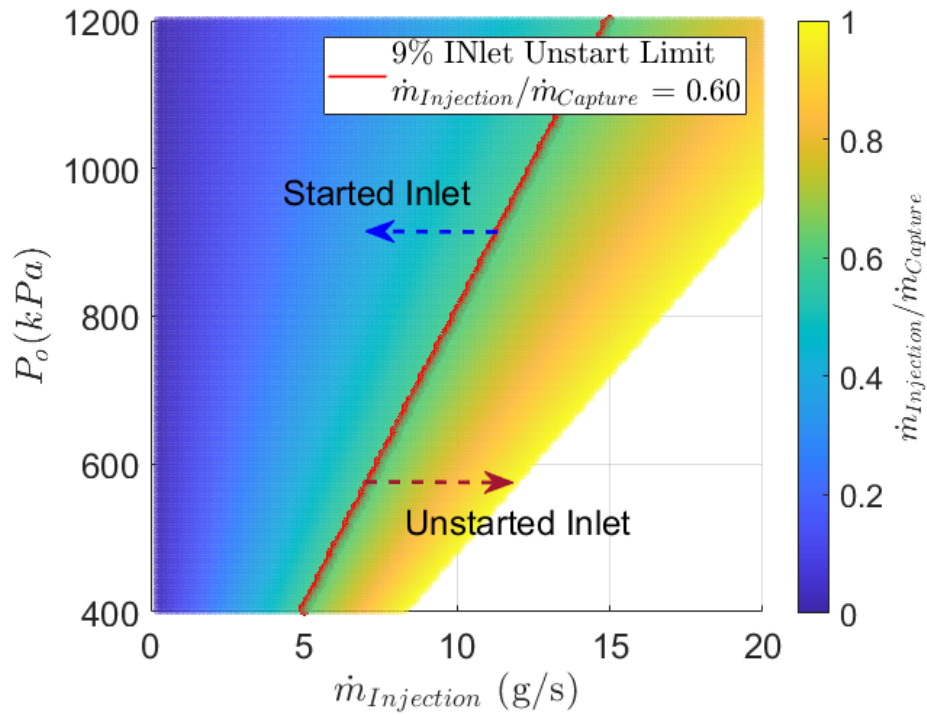
Fig. 13 Extrapolated startability map for the 9% scaled INlet.

5. Power Spectra Results

   A small selection of power spectra were analyzed for the 9% scaled INlet model using Kulite DC-pressure signals. The presented power spectra were calculated over a 0.05 second data segment from Welch's method with a 100 Hz frequency resolution and 50% window overlap. The pressure signal was normalized by the freestream pressure for the time at which the data were recorded. Power spectra provide insight into frequency content of the flow within both the external contraction compression ramp and the isolator. It is expected that flow within the isolator is turbulent due to interactions with the shock train. The effects of mass jet-injection on the state of flow perturbations are shown within this section. The PSDs are shown at two points of time: t = 0.43 seconds where no mass was injected into the isolator and at t = 1.24 seconds during the jet blowing event.

   The first PSD presented in Figure 14 for the fully unstarted 9% INlet case. The Kulites presented on the plot are all within the internal contraction or isolator regions of the inlet. All sensors show highly elevated spectra indicative of turbulent flow. The Kulite sensor located at $X/R_\circ = 15$ shows especially high power of frequency content below 5 kHz. This sensor location sits at the beginning of the internal contraction, which is also where the standing normal shock sits during inlet unstart. A large amount of shock unsteadiness and flow spillage likely contributes to the power in this frequency range. Also, all displayed sensors detect a peak at 2.86 kHz, which is indicative of a universal cavity resonance within the inlet-isolator system.

18
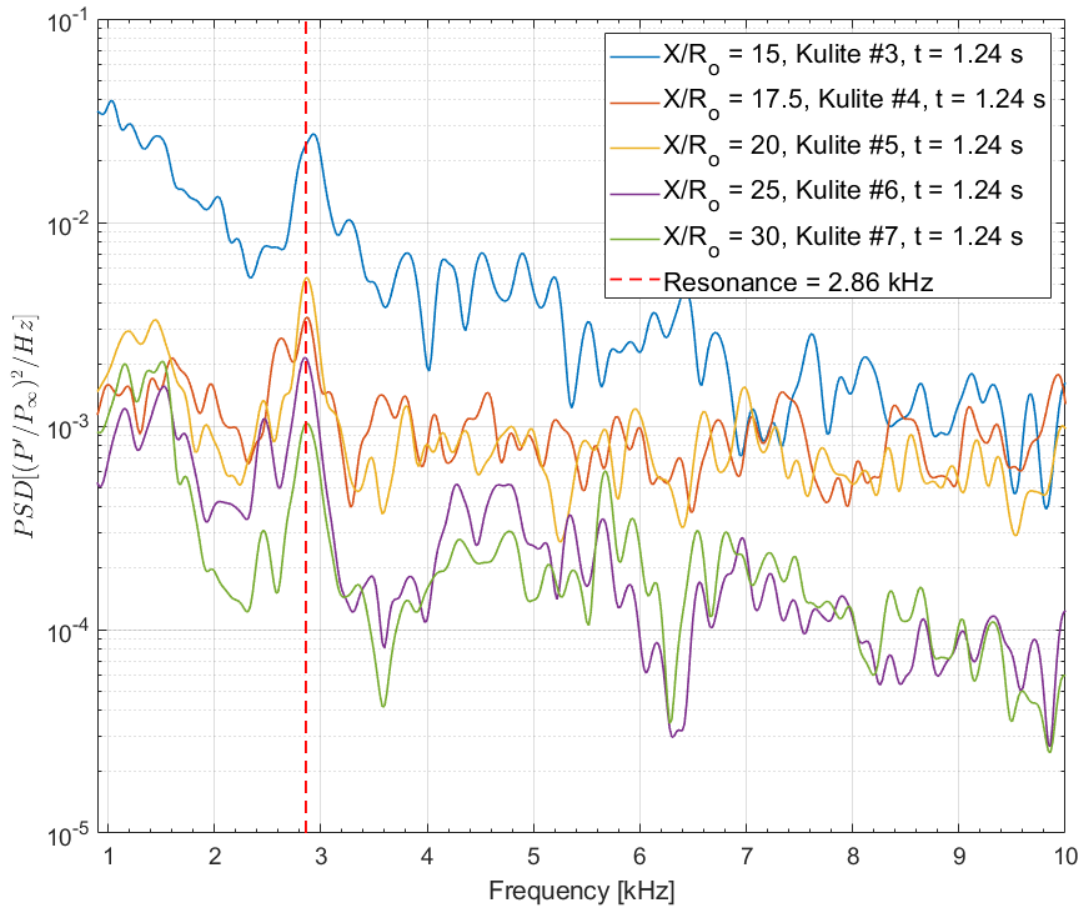
Fig. 14 **Power spectra of internal contraction and isolator Kulites for the 9% scale model during jet-injection. [Mach 6, quiet flow, $P_{\circ,i}$ = 85.2 psia]**

   Power spectra of the external contraction Kulites were also calculated for the same run time and flow condition in Figure 15. Reference PSDs were also calculated and displayed before the unstart event. The pre-unstart PSDs show that signal strength for both Kulites #1 and #2 quickly approaches the noise floor. In this case, the flow in the external contraction is likely laminar. During unstart, the spectra becomes elevated and several distinct peaks become apparent. Although these Kulites are sufficiently upstream, there is acoustic information traveling upstream through the boundary layer during back-pressurization. A peak-finding algorithm was implemented in Matlab to detect the first four peaks at least 200 Hz in width. The results are labeled on the plot.
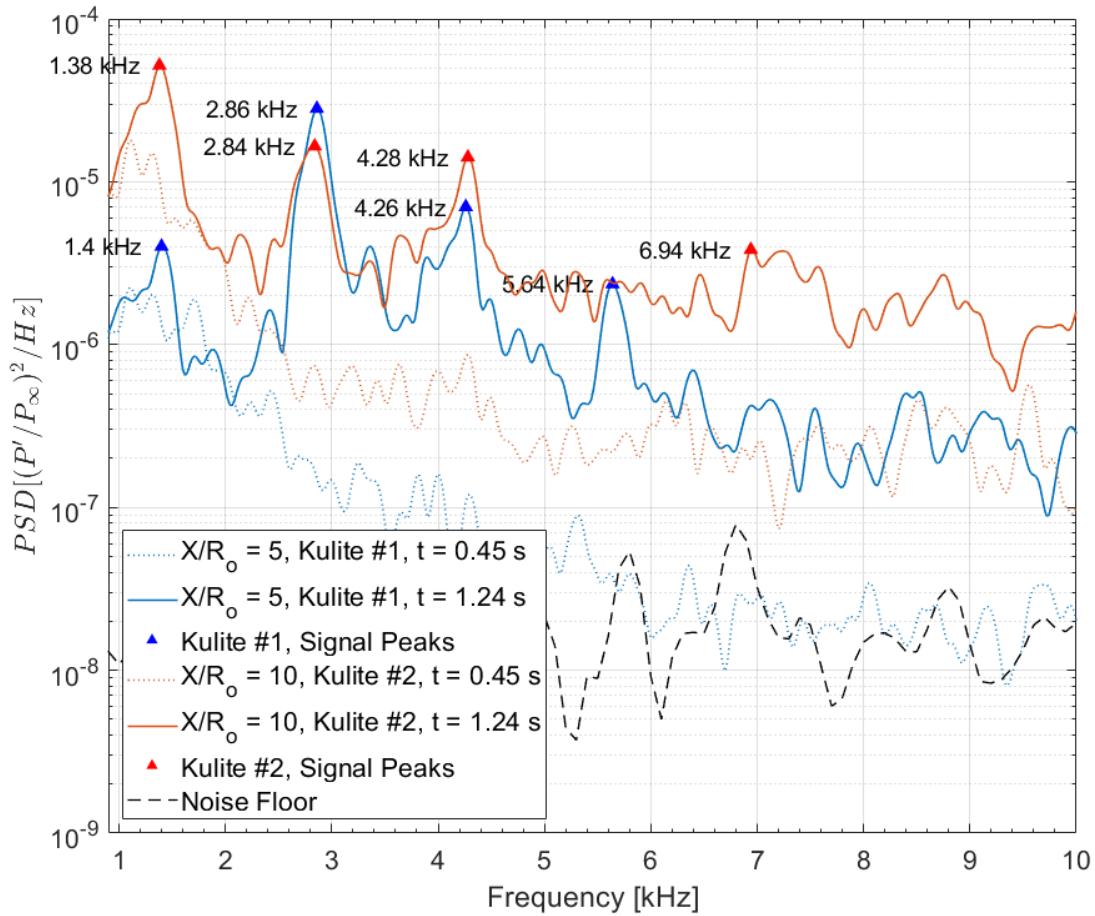
Fig. 15   Power spectra of external contraction Kulites for the 9% scale model before and during jet-injection. [Mach 6, quiet flow, $P_{\circ,i}$ = 85.2 psia]

The peaks detected on the external contraction portion of the inlet are harmonics of the main resonance detected within the isolator. The harmonics likely also exist within the isolator. However, the state of the turbulent boundary downstream makes it hard to discriminate these peaks from the elevated spectral content. A cavity resonance calculation was carried out to determine the theoretical frequencies for an open cavity and its harmonics. The cavity length was was determined by the distance between the start of the internal contraction and the downstream location of the mass-injection port. This port is the beginning of the downstream blockage when airflow is injected within the isolator. Figure 16 shows the cavity distance over a sample INlet model.
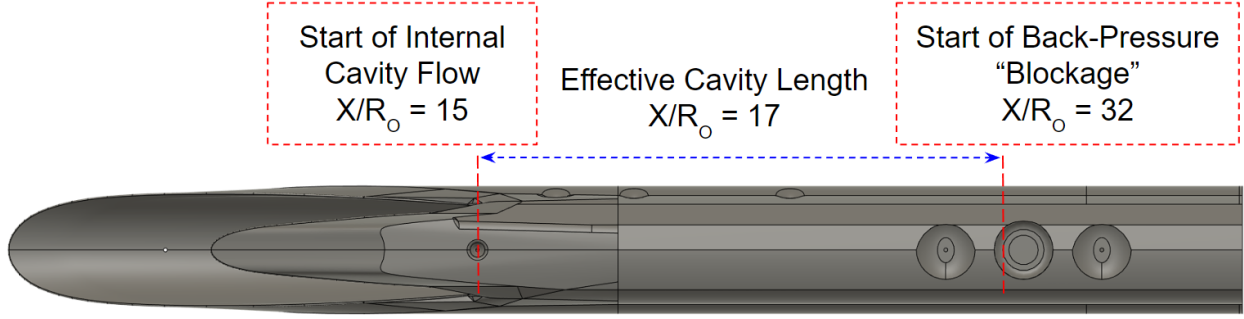
Fig. 16   Definition of the effective cavity length for the INlet model.

Since distance is known from the dimensional throat height for the 9% model ($R_\circ = 0.34$ in., $L = 0.1468$ m), the calculation can be carried out from equation (5). The acoustic speed is calculated from the total temperature within the model's internal boundary layer ($T_t = 425K - 433K$). Both temperatures were used in the calculation to account for uncertainty in the total temperature measurement.

$$f = n\frac{a}{2L} = n\frac{\sqrt{\gamma R T_t}}{2L} \tag{5}$$

Results of the calculations compared with the detected peaks are presented in Table 3. The measured peaks are in good agreement with the calculated even harmonics. Future studies will seek to measure the effect of these cavity resonances on inlet buzz and boundary layer state on the sugar-scoop compression surface.

Table 3   Predicted cavity resonance frequencies for the 9% INlet blockage model.

	Frequencies (kHz)	
n	Predicted	Measured
1	1.41 - 1.42	1.38 - 1.4
2	2.81 - 2.84	2.84 - 2.86
3	4.22 - 4.26	4.26 - 4.28
4	5.63 - 5.68	5.64
5	7.04 - 7.10	6.94

V. Viscous Correction Procedure

In the current version of the code, a boundary layer viscous correction (BLVC) is applied to each inviscid streamline by calculation of the boundary layer displacement thickness (BLDT). This additional process will be utilized in future models and is presented here for completeness. The process used in the design code was developed by Sivells and Payne [30]. Although originally developed for axisymmeric hypersonic wind tunnels with no adverse pressure pressure gradients, the method has been shown to provide a good estimate of boundary layer thickness for streamtraced waverider inlets [31]. The method solves the von-Kármán momentum equation for turbulent axisymmetric boundary layers, which is shown in equation (6). The equation can be solved by a numerical Runge-Kutta scheme similar to the Taylor-Maccoll equations. In the equation, φ is boundary layer momentum thickness, σ is the flow type ($\sigma = 1$ for axisymmetric boundary layers), and γ is the ratio of specific heats. The shape factor (H) is related to the displacement thickness δ^* and momentum thickness by equation (7).

$$\frac{d\varphi}{dx} + \varphi\left[\frac{2 - M_e^2 + H}{M_e(1 + \frac{\gamma-1}{2}M_e^2)}\frac{dM_e}{dx} + \sigma\frac{1}{r}\frac{dr}{dx}\right] = \frac{C_f}{2}sec(\theta) \tag{6}$$

$$H = \frac{\delta^*}{\varphi} \tag{7}$$

21

The original von-Kármán momentum equation is first modified by Stewartson's transformation [32]. These transformations define a relationship between the transformed-incompressible (H_{tr}, φ_{tr}) and compressible (H, φ) flow quantities. They are defined in equations (8) and (9), where T_e is boundary layer edge temperature and $T_\circ$ is stagnation temperature. The relationship is semi-empirical and drawn from wind tunnel correlations, making this method an approximate technique to calculate boundary layer thickness.

$$H = H_{tr}\left(\frac{T_o}{T_e}\right) + \frac{T_o}{T_e} - 1 \tag{8}$$

$$\varphi = \varphi_{tr}\left(\frac{T_o}{T_e}\right)^{\frac{\gamma+1}{2(\gamma-1)}} \tag{9}$$

The stagnation temperature is quantified by its relationship to the edge temperature T_e and edge Mach number M_e in equation (10).

$$T_o = T_e\left(1 + \frac{\gamma - 1}{2}M_e^2\right) \tag{10}$$

The final transformed von-Kármán momentum equation is presented in (11). Properties like transformed shape factor H_{tr}, Mach number, local radius (r), wall angle (θ), and skin friction (C_f) become functions of axial distance. Some values, like edge Mach number (M_e), temperature (T_e), and pressure (P_e) are known from inviscid parameters calculated by the streamtracing routine. To find these quantities, it assumed the freestream flow is Mach 6, freestream stagnation pressure is 160 psia, and freestream stagnation temperature is 433 K. The transformed linear first-order ordinary differential equation takes the form outlined in equation (12), where $P(x)$ and $Q(x)$ are grouped terms representing quantities only a function of axial distance.

$$\frac{d\varphi_{tr}}{dx} + \frac{\varphi_{tr}}{M_e}(2 + H_{tr})\frac{dM_e}{dx} + \sigma\frac{\varphi_{tr}}{r}\frac{dr}{dx} = \frac{C_f}{2}sec(\theta)\left(\frac{T_e}{T_o}\right)^{\frac{\gamma+1}{2(\gamma-1)}} \tag{11}$$

$$\frac{d\varphi_{tr}}{dx} + \varphi_{tr}P(x) = Q(x) \tag{12}$$

Additionally, the transformed shape factor can be computed through a relation that incorporates heat transfer effects when the Prandtl number deviates from unity. The transformed shape (H_{tr}), or "form" factor, is then related to the incompressible flow counterpart (H_i) with Crocco's quadratic for the temperature distribution in the boundary layer. This is shown in equation (13), where T_{aw} is the adiabatic wall temperature.

$$H_{tr} = H_i\left(\frac{T_w}{T_o}\right) + \frac{T_{aw}}{T_o} - 1 \tag{13}$$

The adiabatic wall temperature is defined through a recovery parameter, which is dependent on the Prandtl number (Pr) of the flow. The recovery parameter is defined in equation (14) and the adiabatic wall temperature in (15).

$$\lambda \approx Pr^{1/3} \tag{14}$$

$$T_{aw} = \left(1 + \lambda\frac{\gamma - 1}{2}M_e^2\right) \tag{15}$$

The compressible and incompressible skin-friction coefficients can also be related through the edge and reference temperature (T^*), as shown in equation (16). The method used Eckhert's reference temperature relation, which is equation (17) [33]. The wall temperature (T_w) is a a definable parameter.

$$C_f = \frac{T_e}{T^*}C_{fi} \tag{16}$$

$$T^* = 0.5T_w + 0.22T_{aw} + 0.28T_e \tag{17}$$

Additionally, the shape factor of the incompressible flow can be calculated from the incompressible skin-friction value and shown to reduce into equation (18).

$$H_i = \frac{1}{1 - 7\sqrt{C_{fi}/2}} \tag{18}$$

Next, an approximate method developed by Kármán and Schoenherr to find the average incompressible skin-friction coefficient is introduced in equation (19). The relation is drawn from experimental relations for an approximately adiabatic wall condition. The semi-empirical relation uses the incompressible Reynolds number (Re_X), which is itself defined in equation (20). The skin-friction semi-empirical relation was found to be in good agreement with the data for Reynolds numbers in the range of $10^5 - 10^9$.

$$C_{fi} = \frac{0.088(log_{10}Re_X - 2.3686)}{(log_{10}Re_X - 1.5)^3} \tag{19}$$

$$Re_X = [\frac{\frac{\mu^*Re_x^*}{\mu_o}}{log_{10}\frac{\mu^*Re_x^*}{\mu_o} - 2.3686}][\frac{(log_{10}\frac{\mu^*Re_x^*}{\mu_o} - 1.5)^3}{(log_{10}Re_x^*)^2} - 0.8686] \tag{20}$$

The viscosity term (μ) is definable through Sutherland's law, which is in equation (21).

$$\mu = 1.458 * 10^{-6}\frac{T^{1.5}}{T + 110.4} \tag{21}$$

The incompressible Reynolds number (Re_X) is defined in terms of a reference Reynolds number (Re_x^*) and a length-dependent Reynolds number (Re_x). These relations are defined in (22) and (23).

$$Re_x^* = \frac{T_e}{T^*}\frac{\mu_e}{\mu^*}Re_x \tag{22}$$

$$Re_x = \frac{P_e M_e x}{\mu_e}\sqrt{\frac{\gamma}{RT_e}} \tag{23}$$

Integration of the differential equation proceeds simultaneously with the evaluation of the axial-dependent quantities. Certain conditions may cause numerical instabilities, such as non-continuous boundary layer edge properties or near-zero Reynolds numbers. Sibulkin introduced a distance correction for the Reynolds number during the first integration step [34]. The distance correction is developed for wind-tunnel nozzles and incorporates the local wall radius (r^*) and radius of curvature terms (R^*). This correction was similarly adapted for inlet boundary layer developement along leading edges. The correction is shown in equation (24).

$$x^* = \sqrt{\frac{\gamma + 1}{2}r^*R^*} \tag{24}$$

The streamtracing design code incorporates smooth pressure transitions through shocks and uses the leading-edge correction to avoid numerical instabilities. All streamlines are transformed from a three-dimensional coordinate systems into two-dimensional systems to ease curvature and radial distance calculations. Edge properties are known everywhere and are fed into the Runge-Kutta solver. The calculated displacement thickness is applied in the outward normal direction of each local 2D curve for both the upper and lower surfaces. A 100% displacement thickness correction is used, although the percentage can be altered for future studies to study performance factors. A sample boundary-layer displacement thickness (δ^*) calculation is shown in Figure 17b and implemented in Figure 17a for the center-line $0°$ osculating plane. The adverse pressure gradient causes a slight decrease in the displacement thickness near the throat.

(a) Corrected and uncorrected streamlines.

(b) Boundary-layer displacement thickness profile.
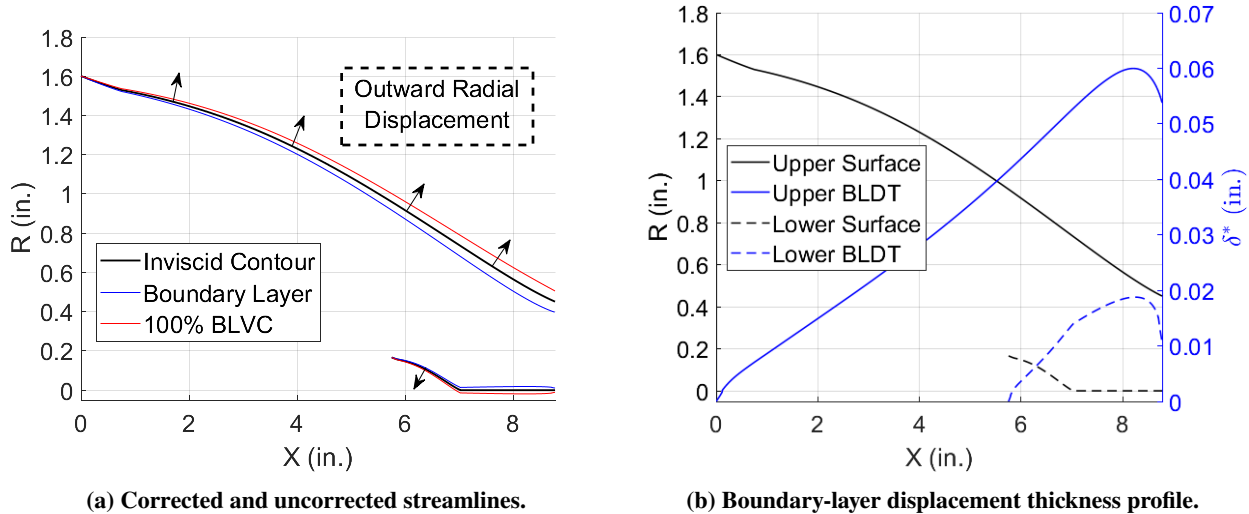
Fig. 17   Boundary layer growth along the $0°$ osculating plane of the 12% scaled INlet for P_o = 160 psia.

The effect of the viscous correction procedure causes a deviation in the inlet's throat profile, as seen in the base plane in Figure 18b. A three-dimensional isometric view of all displaced streamlines can be seen in Figure 18a. Since straight walls in the isolator are preferred for optical access, then a throat transition to a more adequate shape will be required.

(a) Original and corrected INlet shape.

(b) Corrected and uncorrected throat profiles.
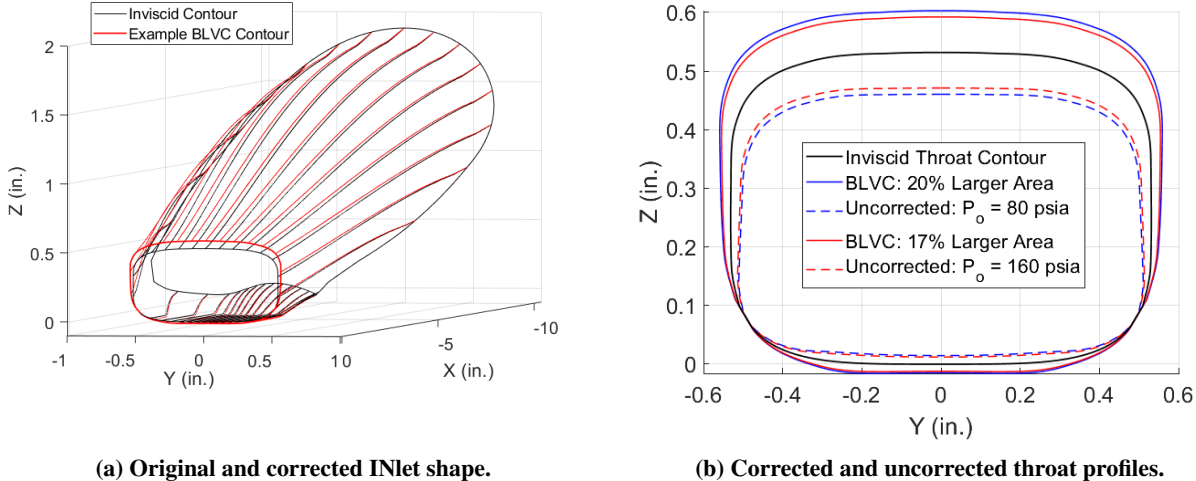
Fig. 18   Examples of an applied viscous correction for the 12% scaled INlet.

VI. Conclusion and Future Work

A discussion of high speed inlet requirements and design methods has been presented. An analytical code for osculating inlet design based on an ICFC flowfield has been written and used to design the blockage models used in this experiment. The starting envelope of the blockage models in the BAM6QT was determined. The improved starting characteristics of the 9% geometry informed the decision to go with a 12% model for future model designs at Purdue University. Comparisons between mean pressures from the 9% and 14% blockage models identified significant differences in performance. The inlet was back-pressured using jet blowing and its effect on flow unsteadiness and capability to cause unstart was quantified. This was utilized to create an unstart map for this inlet at various blowing

ratios. Spectral analysis was used to identify when the inlet was back-pressured and showed evidence of cavity resonance in the inlet. Finally, the methodology and results from a viscous correction were presented and added to the streamtracing code.

Future work will seek to implement the inlet design on more refined models made out of metal with improved diagnostics. Models will be created at Purdue University and a larger scale model will be designed for use in the Air Force Office of Scientific Research Notre Dame Mach-6 Large Quiet Tunnel. Diagnostics such a schlieren imaging, background-oriented schlieren, pressure-sensitive paint, and infrared thermography will be utilized in addition to Kulite and PCB pressure transducers. Extensive investigations of inlet shock train flow physics, back pressure unstart, and angularity effects on the inlet will be conducted experimentally and numerically.

Acknowledgments

References

[1] Heiser, W. H., and Pratt, D. T., *Hypersonic Airbreathing Propulsion*, AIAA, 1994, pp. 197–266. Education Series.

[2] Smart, M. K., "Design of Three-Dimensional Hypersonic Inlets with Rectangular-to-Elliptical Shape Transition," *Journal of Propulsion and Power*, Vol. 15, No. 3, 1999, pp. 408–416. https://doi.org/10.2514/2.5459.

[3] Smart, M., and Ruf, E., "Free-Jet Testing of a REST Scramjet at Off-Design Conditions," *25th AIAA Aerodynamic Measurement Technology and Ground Testing Conference*, AIAA, 2006, p. 1–12. https://doi.org/10.2514/6.2006-2955.

[4] Bulman, M., and Siebenhaar, A., "The Rebirth of Round Hypersonic Propulsion," 2006. https://doi.org/10.2514/6.2006-5035.

[5] You, Y., "An Overview of the Advantages and Concerns of Hypersonic Inward Turning Inlets," 2011. https://doi.org/10.2514/6.2011-2269.

[6] Mölder, S., "Internal, Axisymmetric, Conical Flow." *AIAA Journal*, Vol. 5, No. 7, 1967, pp. 1252–1255. https://doi.org/10.2514/3.4179.

[7] Ogawa, H., Mölder, S., and Boyce, R., "Effects of Leading-Edge Truncation and Stunting on Drag and Efficiency of Busemann Intakes for Axisymmetric Scramjet Engines," *Journal of Fluid Science and Technology*, Vol. 8, No. 2, 2013, pp. 186–199. https://doi.org/10.1299/jfst.8.186.

[8] O'Brien, T., and Colville, J., "Analytical Computation of Leading Edge Truncation Effects on Inviscid Busemann Inlet Performance," *45th AIAA Aerospace Sciences Meeting and Exhibit*, 2007. https://doi.org/10.2514/6.2007-26.

[9] Mölder, S., and Timofeev, E., "Hypersonic Air Intake Design for High Performance and Starting," *RTO-EN-AVT-195*, 2019.

[10] Chang, J., Li, N., Xu, K., Bao, W., and Yu, D., "Recent Research Progress on Unstart Mechanism, Detection and Control of Hypersonic Inlet," *Progress in Aerospace Sciences*, Vol. 89, 2017, pp. 1–22. https://doi.org/https://doi.org/10.1016/j.paerosci.2016.12.001.

[11] Kantrowitz, A., and Donaldson, C., "Preliminary Investigation of Supersonic Diffusers," 1945.

[12] Billig, F., Baurle, R., Tam, C.-J., and Wornom, S., "Design and Analysis of Streamline Traced Hypersonic Inlets," 1999. https://doi.org/10.2514/6.1999-4974.

[13] Sobieczky, H., Dougherty, F., and Jones, K., "Hypersonic Waverider Design from Given Shock Waves." 1990.

[14] Jones, K., and Center, K., "Waverider Design Methods for Non-Conical Shock Geometries," 2002. https://doi.org/10.2514/6.2002-3204.

[15] You, Y., Liang, D., and Cai, K., "Numerical Research of Three-Dimensional Section Controllable Internal Waverider Hypersonic Inlet," 2008. https://doi.org/10.2514/6.2008-4708.

[16] You, Y., and Liang, D., "Design Concept of Three-Dimensional Section Controllable Internal Waverider Hypersonic Inlet," *Science in China Series E: Technological Sciences*, Vol. 52, No. 7, 2009, pp. 2017–2028. https://doi.org/10.1007/s11431-009-0125-1.

[17] Xuzhao, H., Jialing, L., Zheng, Z., Penfei, M., and Yingchuan, W., "Osculating Inward turning Cone Waverider/Inlet (OICWI) Design Methods and Experimental Study," 2012. https://doi.org/10.2514/6.2012-5810.

[18] Hang, Z., and Zhiguang, J., "A Novel Approach for Inverse Design of Three-Dimensional Shock Waves under Non-Uniform Flows," *Acta Astronautica*, Vol. 176, 2020. https://doi.org/10.1016/j.actaastro.2020.06.050.

[19] Flock, A. K., and Gülhan, A., "Viscous Effects and Truncation Effects in Axisymmetric Busemann Scramjet Intakes," *AIAA Journal*, Vol. 54, No. 6, 2016, pp. 1881–1891. https://doi.org/10.2514/1.J054287.

[20] Walsh, P., Tahir, R., and Molder, S., "Boundary-layer Correction for the Busemann Hypersonic Air Inlet," *Canadian Aeronautics and Space Journal*, Vol. 49, 2003, pp. 11–17. https://doi.org/10.5589/q03-003.

[21] Noftz, M. E., Shuck, A. J., Jewell, J. S., Poggie, J., Bustard, A., Juliano, T. J., and Bisek, N. J., *Design of an Internal Osculating Waverider Intake*, chapter and pages. https://doi.org/10.2514/6.2022-0064.

[22] Schneider, S. P., "Development of Hypersonic Quiet Tunnels," *Journal of Spacecraft and Rockets*, Vol. 45, No. 4, 2008, pp. 641–664.

[23] Juliano, T. J., Schneider, S. P., and Aradag, S., "Quiet-Flow Ludwieg Tube for Hypersonic Transition Research," *AIAA Journal*, Vol. 46, No. 7, 2008, pp. 1757–1763.

[24] Chynoweth, B. C., "A New Roughness Array For Controlling the Nonlinear Breakdown of Second-Mode Waves at Mach 6," Master's thesis, Purdue University, January 2015.

[25] Juliano, T. J., Borg, M. P., and Schneider, S. P., "Quiet Tunnel Measurements of HIFiRE-5 Boundary-Layer Transition," *AIAA Journal*, Vol. 53, No. 4, 2015, pp. 832–846.

[26] Pope, A., and Goin, K. L., *"High-speed wind tunnel testing*, Wiley, New York, 1965.

[27] *CE 221*, Freescale Semiconductor, January 2012. Rev F.

[28] Mamrol, D. V., "Characterization of the Quiet Flow Freestream and a Flat Plate Model in the Boeing/AFOSR Mach 6 Quiet Tunnel," Master's thesis, November 2021.

[29] Juliano, T. J., "Nozzle Modifications for High-Reynolds-Number Quiet Flow in the Boeing/AFOSR Mach 6 Quiet Tunnel," Master's thesis, December 2006.

[30] Sivells, J. C., and Payne, R. G., "A Method of Calculating Turbulent Boundary-layer Growth at Hypersonic Mach Numbers," Tech. rep., Arnold Engineering Development Center, Arnold AFB, TN, 1959.

[31] Ding, F., Liu, J., Huang, W., Zhou, Y., and Guo, S., "Boundary-layer Viscous Correction Method for Hypersonic Forebody/Inlet Integration," *Acta Astronautica*, Vol. 189, 2021, pp. 638–657. https://doi.org/https://doi.org/10.1016/j.actaastro.2021.09.018.

[32] Sivells, J. C., "Aerodynamic Design of Axisymmetric Hypersonic Wind-tunnel Nozzles," *Journal of Spacecraft and Rockets*, Vol. 7, No. 11, 1970, pp. 1292–1299. https://doi.org/10.2514/3.30160.

[33] Eckert, E. R., "Survey on Heat Transfer at High Speeds," Tech. rep., University of Minneapolis, 1961.

[34] Sibulkin, M., "Heat Transfer to an Incompressible Turbulent Boundary-layer and Estimation of Heat-transfer Coefficients at Supersonic Nozzle Throats," *Journal of the Aeronautical Sciences*, Vol. 23, No. 2, 1956, pp. 162–172.